machines

MDPI

Article

Inheriting Traditional Chinese Bone-Setting: A Framework of Closed Reduction Skill Learning and Dual-Layer Hybrid Admittance Control for a Dual-Arm Bone-Setting Robot

Zhao Tan [1,2], Jialong Zhang [2], Yahui Zhang [2], Xu Song [2], Yan Yu [2], Guilin Wen [2,*] and Hanfeng Yin [1]

[1] State Key Laboratory of Advanced Design and Manufacture for Vehicle Body, Hunan University, Changsha 410082, China; tanzhao@hnu.edu.cn (Z.T.); yinhanfeng@hnu.edu.cn (H.Y.)
[2] School of Mechanical Engineering, Yanshan University, Qinhuangdao 066004, China; zjl1127@stumail.ysu.edu.cn (J.Z.); zhangyahui@ysu.edu.cn (Y.Z.); xsong@stumail.ysu.edu.cn (X.S.); yy2001@stumail.ysu.edu.cn (Y.Y.)
* Correspondence: glwen@ysu.edu.cn

Abstract: Traditional Chinese Bone-setting (TCB) involves complex movements and force feedback, which are critical for effective fracture reduction. However, its practice necessitates the collaboration of highly experienced surgeons, and the availability of expert resources is significantly limited. These challenges have significantly hindered the inheritance and dissemination of TCB techniques. The advancement of Learning from Demonstration offers a promising solution for addressing this challenge. In this study, we developed an innovative framework of closed reduction skill learning and dual-layer hybrid admittance control for a dual-arm bone-setting robot, specifically targeting ankle fracture. The framework began with a comprehensive structural design of the robot, incorporating analyses of closed-chain kinematics and the decomposition of internal and external forces. Additionally, we introduced a globally optimal reparameterization algorithm for temporal alignment of demonstrations and extended the Motion/Force Synchronous Kernelized Movement Primitive to learn reduction maneuvers and forces. Furthermore, we designed a dual-layer hybrid admittance controller, consisting of an ankle-layer and a robot- layer. Specifically, we propose a novel adaptive fuzzy variable admittance control strategy for the ankle-layer to achieve accurate tracking of reduction forces, which reduces the RMSE of force tracking along the X-axis by 50.35% compared to the non-fuzzy strategy. The experimental results demonstrated that the framework successfully replicates the human-like bone-setting process and can imitate personalized bone-setting trajectories under expert guidance.

Keywords: traditional Chinese bone-setting; ankle; dual-arm robot; learn from demonstration; adaptive admittance control

check for updates

Academic Editor: Dan Zhang

Received: 24 March 2025
Revised: 21 April 2025
Accepted: 28 April 2025
Published: 29 April 2025

Citation: Tan, Z.; Zhang, J.; Zhang, Y.; Song, X.; Yu, Y.; Wen, G.; Yin, H. Inheriting Traditional Chinese Bone-Setting: A Framework of Closed Reduction Skill Learning and Dual-Layer Hybrid Admittance Control for a Dual-Arm Bone-Setting Robot. *Machines* **2025**, *13*, 369. https://doi.org/10.3390/machines13050369

Copyright: © 2025 by the authors. Licensee MDPI, Basel, Switzerland. This article is an open access article distributed under the terms and conditions of the Creative Commons Attribution (CC BY) license (https://creativecommons.org/licenses/by/4.0/).

1. Introduction

Fracture reduction is a critical step in orthopedic treatment. Robotic systems developed for open or minimally invasive procedures have attracted substantial attention and have been extensively reviewed [1–3]. However, they tend to overlook closed reduction techniques, particularly Traditional Chinese Bone-setting (TCB), which remains underexplored in robotics despite its established clinical efficacy [4]. TCB is a non-invasive manual technique where practitioners realign fractured bones using tactile feedback, anatomical knowledge, and clinical experience [5,6]. It is commonly applied to fractures of the radius, hip, ankle, and other bones. Among various fractures, ankle fractures are particularly

noteworthy due to their high incidence and sensitivity to treatment. Compared with open surgery, closed ankle fracture reduction offers benefits such as reduced trauma, faster recovery, and lower cost. In high-energy trauma cases, it also helps prevent surgical delays and lowers the risk of post-traumatic arthritis [7,8]. Nevertheless, TCB has limitations. It depends heavily on the practitioner's strength and subjective expertise, which are difficult to quantify or standardize. The lack of structured training programs further impedes the transmission of these complex skills. Therefore, intelligent robotic platforms capable of digitizing and automating TCB techniques are urgently needed.

Unlike conventional trajectory planning methods commonly used in fracture reduction robots, such as A* algorithm [9,10], Learning from Demonstration (LfD) is a class of learning methods that enables robots to acquire human-like skills by leveraging a limited number of expert demonstrations [11–17]. Moreover, compared with imitation learning methods such as behavior cloning [18,19] and imitation reinforcement learning [20,21], LfD offers better sample efficiency and avoids extensive iterative training. Popular models include Dynamic Movement Primitives (DMP) [22,23], Probabilistic Movement Primitives (ProMP) [24], Stable Estimator of Dynamical Systems (SEDS) [25], Kernelized Movement Primitives (KMP) [26,27], and Probabilistically informed Motion Primitives [28]. In rehabilitation robotics, Wu et al. [29] proposed MF2RoSL, a framework based on manifold mapping and Gaussian processes for skill acquisition, while Zou et al. [30] developed learning-based gait models to reconstruct walking patterns from healthy subjects. Liu et al. [31] introduced Posture-Synergy Kernelized Movement Primitives (PSKMP) to enable humanoid trajectory planning for upper-limb rehabilitation. In surgical applications, Pan et al. [32] employed discrete DMP to digitize physician-performed reduction motions. Bian et al. [33] modeled implicit constraints in minimally invasive procedures using probabilistic representations to resolve Remote Center of Motion (RCM) inconsistencies. Zhang et al. [34] developed an appendectomy system based on DMP-learned surgical motions. Schwaner et al. [35] utilized Surgical action primitives to realize fully autonomous bi-manual suturing. Hang et al. [36] transferred motion skills from open surgery to robot-assisted minimally invasive systems using Dynamic Time Warping (DTW) and DMP. Despite these advances, most existing studies still rely on DTW for trajectory alignment, which requires manually selecting a reference trajectory. In addition, many applications focus on learning motion in low-dimensional translational space, with limited attention to the coordination between motion and force. These limitations reduce their effectiveness in tasks such as fracture reduction, which demand precise and responsive control of both position and force.

Impedance and admittance control strategies, which rely on virtual mass–spring–damper models to regulate a robot's response to external forces [37,38], have been widely applied across various robotic systems [39–43]. For fracture reduction, Zheng et al. [44,45] addressed system nonlinearities through fuzzy adaptive sliding-mode control. Other advances include hierarchical impedance strategies for exoskeletons [46], parameter tuning via inverse reinforcement learning [47], and online stiffness regulation using quadratic programming [48]. Dual-arm robots, capable of bimanual coordination and distributed force application, are particularly well suited for surgical scenarios [1,49–52]. For example, Bai et al. [53] introduced an anthropomorphic control strategy, and Ferraguti et al. [54] enhanced system stability using an energy-tank-based controller. Further improvements were achieved through dual-master/single-slave impedance schemes [55]. Despite these developments, implementing compliant dual-arm control under closed-chain constraints remains challenging, particularly when object properties are uncertain. Recent efforts have explored symmetric admittance control [56], hybrid impedance frameworks [57], and absolute–relative motion control for dynamic grasping tasks [58]. However, most of these approaches emphasize unidirectional or static force tracking. Few studies have focused on

the real-time synchronization of multi-axis motion and force, which is critical for dynamic bone-setting procedures. Moreover, the impact of coefficient selection in adaptive control strategies on system stability is often underestimated [56,57].

To address the challenges of synchronized imitation learning of multi-dimensional motion-force trajectories and adaptive dual-arm cooperative control for the bone-setting robot, this study developed an innovative framework of closed reduction skill learning and dual-layer hybrid admittance control for ankle fracture. The main contributions are as follows:

(1) Motion/Force Synchronous Kernelized Movement Primitives with Globally Optimal Reparameterization Algorithm (GORA) trajectory alignment is extended to learn TCB-based reduction maneuvers and forces.
(2) A dual-layer hybrid admittance control framework is proposed to achieve precise multi-axis force tracking under closed-chain constraints, featuring an ankle-layer adaptive fuzzy variable admittance control and a robot-layer admittance control. In particular, a fuzzy strategy is employed to dynamically adjust the coefficient in adaptive stiffness control law, thereby enhancing force tracking accuracy.
(3) A dual-arm robotic bone-setting platform is developed and validated, demonstrating the effectiveness and robustness of the proposed control framework in reproducing TCB skills with high force-tracking accuracy.

The remainder of this paper is organized as follows. Section 2 describes the system model of the dual-arm bone-setting robot. Section 3 explains the Motion/Force Synchronous kernelized movement primitive to learn the maneuvers and forces used in TCB. Section 4 introduces the design of the dual-layer hybrid admittance controller. Section 5 introduces the experimental setup and experiment results. The conclusions and future work are given in Section 6.

2. System Model of Dual-Arm Bone-Setting Robot

As shown in Figure 1, an experimental platform for dual-arm bone-setting is established, consisting primarily of a dual-arm robot, a fixation boot, an adjustable calf support, silicone prosthetic limb, and a monitoring system. Subsequently, we conducted kinematic and force analysis of the dual-arm robot under closed-chain constraints. It is important to point out that the selection of the dual-arm structure is based on two considerations. First, it provides a more stable mechanical configuration and higher load capacity. Second, the anthropomorphic design of the arms aligns with the need for human-like bone-setting. Moreover, the dual-arm bone-setting robot in this study establishes a flexible, non-invasive connection to the injured limb through a custom-designed fixation boot.

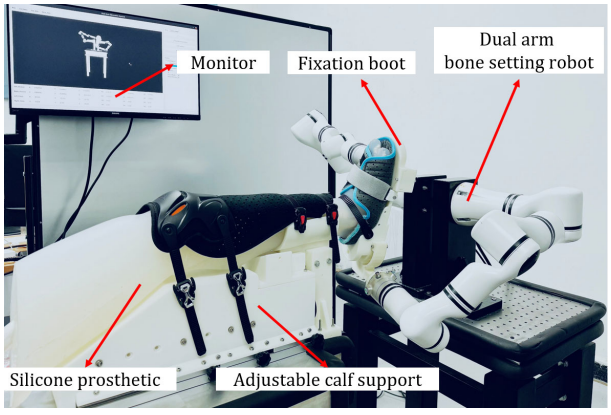

Figure 1. Schematic diagram of dual-arm bone-setting robot.

2.1. Kinematic Analysis of Dual-Arm Robot

During the bone-setting procedure, the dual-arm robot maintains a fixed connection with the patient's ankle, requiring a constant relative pose between the arms and the ankle to ensure operational accuracy and safety. To achieve this, a closed-chain kinematic model is constructed to define the constraint relationships among the two arms and the ankle. Based on this model, the expert-demonstrated reduction trajectory is transformed into executable motion trajectories for the dual-arm system. The kinematic structure of the robot is illustrated in Figure 2a.

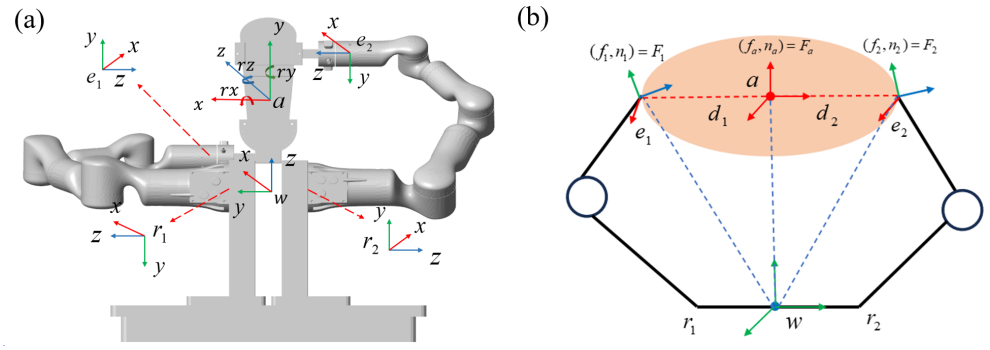

Figure 2. The model of dual-arm bone-setting robot. (**a**) The diagram of the dual-arm bone-setting robot kinematic model. (**b**) The force distribution diagram of the closed-chain constraints model of the dual-arm bone-setting robot.

The coordinate system involved in the kinematic model is defined in Table 1. The expression for converting the given ankle reduction trajectory into the form of a homogeneous transformation matrix is ${}^{w}T_{a}(t)$, which can be described as

$$ {}^{w}T_{a}(t) = \begin{bmatrix} {}^{w}R_{a}(t) & {}^{w}p_{a}(t) \\ 0 & 1 \end{bmatrix} \tag{1} $$

where ${}^{w}R_{a}(t)$ represents the 3×3 rotation relationship of the ankle coordinate system relative to the world coordinate system; ${}^{w}p_{a}(t)$ represents the 3×1 position relationship of the ankle coordinate system relative to the world coordinate system.

Table 1. Description of coordinate system.

Symbol	Description
w	The world frame of the system
a	The ankle frame of the system
r_1	The base coordinate frame of the left robot arm
r_2	The base coordinate frame of the right robot arm
e_1	The end coordinate frame of the left robot arm
e_2	The end coordinate frame of the right robot arm

In this study, the world coordinate system is set between the bases of the dual-arm robot. Therefore, it is easy to know that the relative pose relationship ${}^{w}T_{r_u}$ between the world coordinate frame w and the base coordinate frame r_u of the dual-arm robot remains unchanged. During the cooperative orthopedic process, there is no relative motion between the dual-arm robot and the ankle, so there is also no relative pose transformation between the end-effector coordinate frame e_u of the robots and the ankle frame a. Hence, ${}^{e_u}T_{a}$ is also a constant.

Based on the closed-chain constraint conditions formed by the dual-arm robot and the ankle, the pose constraint relationship can be obtained as follows:

$$^{w}T_{a} = {}^{w}T_{r_u}\,{}^{r_u}T_{e_u}\,{}^{e_u}T_{a}\ (u = 1, 2) \tag{2}$$

where $^{w}T_{a}$ represents the transformation matrix of the ankle coordinate frame relative to the world coordinate frame, $^{w}T_{r_u}$ represents the transformation matrix of the base coordinate frame robot r_u relative to the world coordinate frame, $^{r_u}T_{e_u}$ represents the transformation matrix of the end-effector coordinate frame of the robot e_u relative to its base coordinate frame robot r_u, and $^{e_u}T_{a}$ represents the transformation matrix of the ankle coordinate frame relative to the end-effector coordinate frame of the robot e_u.

$$^{r_u}T_{e_u} = \left({}^{w}T_{r_u}\right)^{-1}{}^{w}T_{a}\left({}^{e_u}T_{a}\right)^{-1}\ (u = 1, 2) \tag{3}$$

According to the formula, the transformation matrix of the end-effector coordinate frame of the robot e_u relative to the base coordinate frame robot r_u can be obtained, which represents the motion trajectory of the dual-arm robot. Finally, the joint motion of the *u-th* robot could be computed by solving the inverse kinematics as

$$\theta_u = f_{ikine}\left({}^{r_u}T_{e_u}\right) \tag{4}$$

where $f_{ikine}(\cdot)$ is the inverse kinematics solution of the robot.

2.2. Analysis of Internal and External Force Decomposition

In the process of TCB, in addition to paying attention to the reduction trajectory, it is also crucial to conduct a detailed analysis of the applied forces. Excessive interactive force may not only cause discomfort to patients, but also lead to iatrogenic damage. Therefore, it is very necessary to carry out mechanical analysis on dual-arm robots under closed-chain constraints. Firstly, based on the closed-chain constraints model of the dual-arm bone-setting robot, we allocate the expected force acting on the ends of both arms. The force distribution diagram of the closed-chain constraints model of the dual-arm bone-setting robot is shown in Figure 2b. In this model, the expected force at the ankle can be represented by the Newton–Euler method:

$$\begin{cases} f_a = M_a\ddot{c} - M_a g \\ n_a = \ I_a\dot{\omega} + \omega \times \ I_a\omega \end{cases} \tag{5}$$

where f_a and n_a denote the desired force and torque exerted on the ankle, respectively. The mass of the ankle is represented by M_a, while $\ddot{c}$ indicates its acceleration. The term g corresponds to the gravitational acceleration, and I_a signifies the inertia matrix of the ankle. Furthermore, ω and $\dot{\omega}$ represent the angular velocity and angular acceleration about the ankle, respectively.

As shown in Figure 2b, the force at the ankle can also be calculated by the force at the end of the arms. Therefore, the following equation can be obtained:

$$\begin{cases} f_a = \sum_{u=1}^{2} f_u \\ n_a = \sum_{u=1}^{2} n_u + \sum_{i=1}^{2} d_u \times f_u \end{cases} \tag{6}$$

where f_u and n_u are the force and torque applied to the ankle using the *u-th* arm. d_u represents the distance from the end of the *u-th* arm to the ankle in the ankle coordinate system.

Based on [56–59], Equation (5) can be converted into:

$$F_a = G\hat{F} \tag{7}$$

where $F_a = [f_a, n_a]^T$ represents the generalized forces exerted on the ankle, and the forces being imparted by the dual-arm robot are

$$\hat{F} = [F_1, F_2]^T = \left[{f_1}^T, {n_1}^T, {f_2}^T, n_2^T\right]^T \tag{8}$$

and the grasp matrix is defined as $G = \begin{bmatrix} I_3 & 0_3 & I_3 & 0_3 \\ S(d_1) & I_3 & S(d_2) & I_3 \end{bmatrix}$, with

$$S(d_i) = \begin{bmatrix} 0 & -d_{iz} & d_{iy} \\ d_{iz} & 0 & -d_{ix} \\ -d_{iy} & d_{ix} & 0 \end{bmatrix} \tag{9}$$

$$d_i = \begin{bmatrix} d_{ix} & d_{iy} & d_{iz} \end{bmatrix} \tag{10}$$

where I_3 is the 3×3 identity matrix, and 0_3 is the 3×3 zero matrix.

In practical applications, the desired force at the ankle is known and must be effectively mapped to the end-effectors of both arms. This mapping enables the robot to apply appropriate forces and torques to the ankle, ensuring accurate tracking of the target force. This task corresponds to solving the inverse problem of Equation (7), commonly referred to as the force allocation problem.

The key challenge lies in transforming the desired ankle force into the corresponding force and torque that should be exerted by each arm. Since the grasping matrix involved is non-square, the inverse problem admits infinitely many solutions. Consequently, Equation (7) can be reformulated as

$$\hat{F} = G^+ F_a + \left(I_{12} - G^+ G \right)\varepsilon \tag{11}$$

where $G^+ = AG^T\left(GAG^T\right)^{-1}$, A is a positive definite matrix, ε is an arbitrary vector. Obviousness G is a right inverse matrix; it satisfies $GG^+ = I$. Therefore, we can obtain

$$\begin{aligned} GF &= GG^+ F_a + G(I_{12} - G^+ G)\varepsilon \\ &= GAG^T\left(GAG^T\right)^{-1} F_a + G(I_{12} - G^+ G)\varepsilon \\ &= F_a \end{aligned} \tag{12}$$

From Equation (12), it can be seen that $(I_{12} - G^+ G)\varepsilon$ does not affect the expected force of the ankle, indicating that the internal force generated between the ankle and each arm only exists in the zero space of the grasp matrix. Here, $G^+ F$ represents the expected external force required to drive the dual-arm robot to track the desired force on the ankle. Based on the "non-squeezing" pseudo inverse principle, we can add a virtual constraint between the dual-arm robot and ankle to form a complete system. Therefore, based on the conclusions of references [56–59], we can represent A as

$$A = \begin{bmatrix} 0_3 & kI_3 & 0_3 & 0_3 \\ kI_3 & 0_3 & 0_3 & 0_3 \\ 0_3 & 0_3 & 0_3 & kI_3 \\ 0_3 & 0_3 & kI_3 & 0_3 \end{bmatrix} \tag{13}$$

where k is any arbitrary non-zero number. Substituting A into the inverse formula yields

$$G^{+} = \begin{bmatrix} I_3 & 0_3 \\ -(Sd_1) & I_3 \\ I_3 & 0_3 \\ -(Sd_2) & I_3 \end{bmatrix} \tag{14}$$

From $GG^{+} = I$, it can be concluded that the pseudoinverse G^{+} satisfies the condition. Based on the above reasoning, the force information acting on the ankle can be transformed into the required driving expected forces for each arm through force distribution. Noting that, we only consider maintaining stability between the arms and the ankle in this study, without considering internal forces. Therefore, the expression for the expected forces is as follows:

$$\begin{cases} F_{Ed} = G^{+}F_a \\ F_{Id} = 0 \end{cases} \tag{15}$$

where F_{Ed} represents the expected external force, and F_{Id} represents the expected internal force. We collect the actual resultant force applied by the arm through a six-dimensional force sensor at the end of the arm. Therefore, it is necessary to decompose this resultant force into two parts; one is the actual external force that drives the dual-arm robot to track the expected force of the ankle, and the other is the actual internal force between the ankle and each arm. Its expression can be expressed as

$$\begin{cases} F_{Er} = G^{+}GF_r \\ F_{Ir} = (\ I_a - G^{+}G)F_r \end{cases} \tag{16}$$

where F_{Er} and F_{Ir} represent the transformation of values obtained from the six-dimensional force sensor at the arm's terminus into external and internal forces, respectively. Meanwhile, F_r signifies the actual measurements acquired from the six-dimensional force sensor at the end of the dual-arm system. Utilizing the derived F_{Er} and F_{Ir}, we can track the desired expected external force F_{Ed} and expected internal force F_{Id} necessary for the operation on the object.

3. Personalized Bone-Setting Skill Imitation Learning

Unlike the existing studies that rely on path planning algorithms such as A* or RRT without learning capabilities [9,10], this study focuses on the synchronized imitation learning of both motion and force trajectories in ankle bone-setting. To account for personalized trajectory learning and generalization, we adopt GORA for temporal alignment and extend the KMP framework by proposing a Motion/Force Synchronous Kernelized Movement Primitive.

3.1. Demonstration Acquisition and Preprocessing

Traditional Chinese Bone-setting (TCB), a long-standing clinical technique within Traditional Chinese Medicine, involves manual manipulations such as palpation, realignment, lifting, traction, and pushing to restore proper anatomical alignment of dislocated bones and joints [4,5]. This study focuses specifically on anatomically precise reduction maneuvers, excluding massage or pressure-based techniques, with an emphasis on the realignment of the tibia, fibula, and talus in ankle dislocation fractures.

To capture expert demonstrations with high fidelity, we developed a bone-setting data acquisition platform comprising a custom-designed acquisition shoe, two six-dimensional (6D) force sensors (Nordbo Robotics, Odense, Denmark) with a frequency of 1000 Hz, and an optical motion tracking system (AIMOOE, Guangzhou, China) operating at 60 Hz. The shoe is non-invasively fixed to the patient's foot using medical-grade straps, and its movement trajectory is used to represent foot motion during reduction (Figure 3a). A custom software platform aligns force and motion data streams in time, ensuring accurate synchronization across modalities. For validation, anatomically realistic silicone prosthetic models were fabricated based on CT scans of supination-type fracture cases, under the supervision of orthopedic specialists. The complete acquisition setup is illustrated in Figure 3b. This system enables precise, synchronized recording of motion and force signals, providing a robust foundation for data-driven modeling and learning of expert bone-setting techniques.

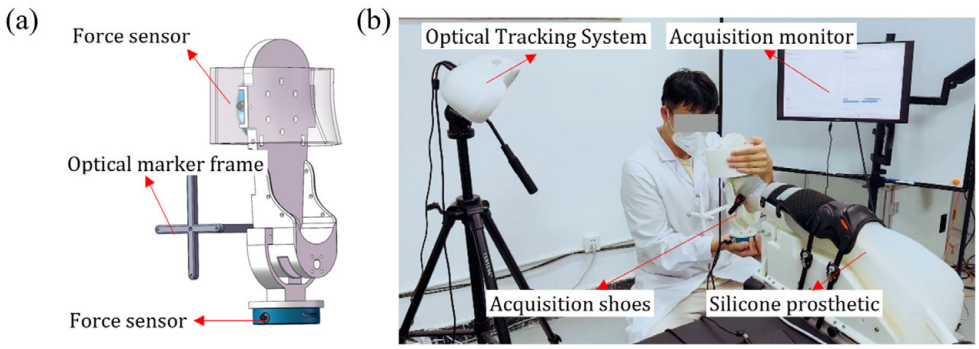

Figure 3. Schematic diagram of the acquisition platform. (**a**) Acquisition shoe. (**b**) Bone-setting data acquisition platform.

Two experienced TCB surgeons participated in the reduction demonstrations. Each surgeon performed six repetitions of the reduction procedure on the homemade silicone prosthetic bone fracture model, generating a total of twelve expert demonstration datasets. Each dataset includes displacement, orientation, and the forces and torques recorded by the two 6D force sensors. After synchronizing and processing the data via software, an expert demonstration dataset was created. Under clinical guidance, the bone-setting process can be divided into six key movements: Traction, Eversion, Anterior Rotation, Lifting, Plantarflexion, and Fixation (Figure 4). Notably, Traction typically requires substantial loads. This serves two purposes, that is, facilitating subsequent reduction maneuvers by separating the tibia, fibula, and talus, and relaxing the surrounding soft tissues to alleviate pressure. The variations in force during the Traction process embody the essence of TCB techniques. Furthermore, actions such as eversion, anterior rotation, lifting, and plantarflexion rely heavily on the practitioner's experience to guide orientation adjustments during reduction. These adjustments play a critical role in determining the overall success of the treatment.

Prior to performing imitation learning, temporal alignment of demonstration trajectories serves as a critical preprocessing step. Although different demonstrations may share similar spatial patterns, variations in execution speed introduce temporal inconsistencies, complicating probabilistic modeling. To address this, trajectory time axes must be reparameterized to ensure alignment on a consistent temporal scale. Traditional approaches often rely on DTW [60], which aligns trajectories by deforming them to match a chosen reference. However, this reliance on a single reference can introduce bias and result in suboptimal alignment. In contrast, we adopt GORA [28,61], a variational method that computes globally optimal temporal alignment across all trajectories. By eliminating reference

bias, GORA enables more accurate and consistent modeling of synchronized motion and force trajectories in demonstrations.

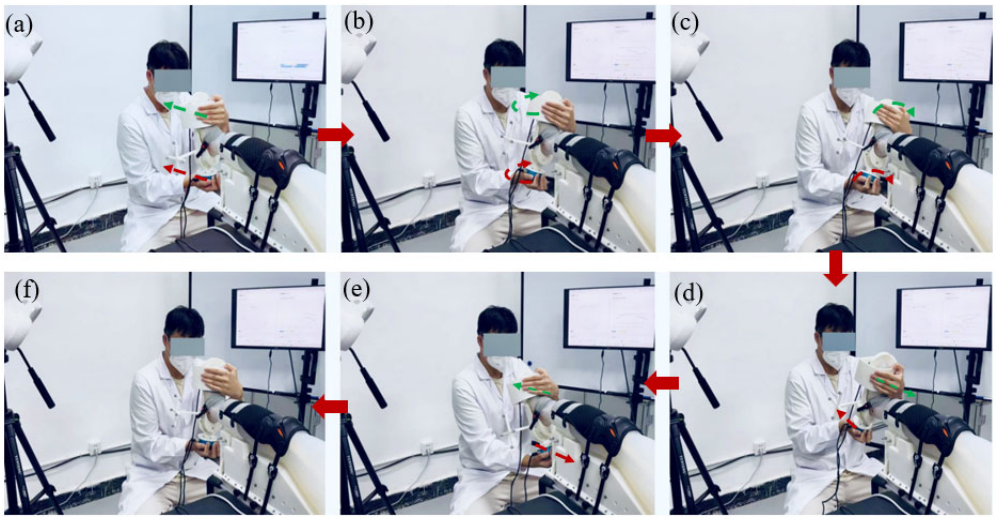

Figure 4. Bone-setting process. (**a**) Traction. (**b**) Eversion. (**c**) Anterior Rotation. (**d**) Lifting. (**e**) Plantarflexion. (**f**) Fixation.

Here, we perform time alignment for the motion trajectory SE(3) sequence and the reduction force sequence, respectively. Consider a sequence in the special Euclidean group SE(3), represented as $G(\tau)$ and parameterized by $\tau \in [0,1]$. Here, $\tau(t) : [0,1] \to [0,1]$ is a monotonically increasing function representing time. The total variation of this sequence is computed as the integral of the squared derivative with respect to time t:

$$\mathcal{J} = \int_0^1 \mathcal{F}(\tau, \dot{\tau})dt = \int_0^1 \mathcal{G}(\tau)\dot{\tau}^2 dt \tag{17}$$

where $\dot{\tau} = d\tau/dt$. The functional $\mathcal{F}(\tau, \dot{\tau})$ outlines the general form of our variational problem, and $G(\tau)$ is structured to ensure global optimality. Specifically, $\mathcal{G}(\tau)$ is expressed based on the body velocity of an SE(3) trajectory,

$$\mathcal{G}(\tau) = \|G^{-1}\frac{\partial G}{\partial \tau}\|_W^2 \tag{18}$$

The weighted Frobenius norm $\|\cdot\|_W$ for a matrix $\mathcal{S} \in \mathbb{R}^{4\times4}$ is given by $\|\mathcal{S}\|_W = \sqrt{tr(\mathcal{S}^T W \mathcal{S})}$, with the weight matrix W defined as

$$W = \begin{pmatrix} 1/2tr(I_m)\mathbb{I}_3 & 0 \\ 0^T & 1 \end{pmatrix} \in \mathbb{R}^{4\times4} \tag{19}$$

where I_m is the 3×3 diagonal inertia tensor for a unit mass solid sphere, and $\mathbb{I}_3$ is the identity matrix.

The integral form $\mathcal{G}(\tau)$ is specifically designed to achieve global optimality by minimizing the weighted norm of the body velocity over the parameter τ. The minimization is performed using the Euler–Lagrange equation:

$$\frac{\partial \mathcal{F}}{\partial \tau} - \frac{d}{dt}\left(\frac{\partial \mathcal{F}}{\partial \dot{\tau}}\right) = 0 \tag{20}$$

By solving this equation with the given structure of $\mathcal{G}(\tau)$, we derive a globally minimal solution, that is:

(1) The integrand $\mathcal{G}(\tau)$ conforms to the defined structure.
(2) The function $\tau : [0,1] \to [0,1]$ is monotonic with $\tau(0) = 0$ and $\tau(1) = 1$.

The optimal reparameterization is found to be $\tau^*(t) = \mathbb{F}^{-1}$. Here,

$$\mathbb{F}(\tau^*) = \frac{\int_0^{\tau^*} \mathcal{G}^{1/2}(\delta)d\delta}{\int_0^1 \mathcal{G}^{1/2}(\delta)d\delta} = t \tag{21}$$

where $\mathbb{F}^{-1}(\cdot)$ is the inverse of $\mathbb{F}$. This reparameterization method, based on variational calculus, ensures the temporal alignment of demonstrated trajectories on a unified time scale. Such alignment is essential for consistent feature representation, enabling more robust probabilistic modeling and accurate imitation learning. By addressing temporal inconsistencies, this approach yields a globally optimal solution that can improve the reliability of trajectory learning in imitation contexts.

3.2. Probabilistic Modeling of the Demonstrations

Formally, we denote the set of demonstrated bone-setting data by

$$\left\{ \left\{ t_n, \mathcal{g}_{h,n} \right\}_{h=1}^{H} \right\}_{n=1}^{N} \tag{22}$$

where t_n represents the n-th time step, $\mathcal{g}_{h,n}$ represents the h-th I-dimensional input and O-dimensional output vectors of the n-th demonstration in the database. N and H denote the length of each demonstration and the number of demonstrations in the database, respectively. Here, $\mathcal{g}_{h,n}$ can be expressed as follows:

$$\mathcal{g}_{h,n} = \left[p, \vartheta, F, M, \dot{p}, \dot{\vartheta}, \dot{F}, \dot{M} \right]^{\mathrm{T}} \tag{23}$$

where p and $\dot{p}$ represent the position and velocity, while ϑ and $\dot{\vartheta}$ denote the Euler angles and angular velocities. F and $\dot{F}$ represent the reduction force and its rate of change; M and $\dot{M}$ indicate the reduction torque and its rate of change.

To enhance the adaptability of the learned trajectory, we introduce a probabilistic framework that characterizes the trajectory's inherent distribution through the approximation GMM, which is defined as

$$P_b(t|\mathcal{g}) \approx \sum_{c=1}^{C} \pi_c \mathbb{N}(t|\mu_c, \Sigma_c) \tag{24}$$

where C represents the number of Gaussian components, π_c denotes the prior probabilities, and $\mathbb{N}(t|\mu_c, \Sigma_c)$ are the Gaussian distributions characterized by mean μ_c and covariance Σ_c. The parameters of the Gaussian Mixture Model (GMM) are estimated using the expectation-maximization (EM) algorithm. The joint probability distribution encoded by the GMM can be expressed as

$$\mu_c = \begin{bmatrix} \mu_c^t \\ \mu_c^D \end{bmatrix}, \ \Sigma_c = \begin{bmatrix} \Sigma_c^{tt} & \Sigma_c^{tD} \\ \Sigma_c^{Dt} & \Sigma_c^{DD} \end{bmatrix} \tag{25}$$

The conditional expectation for a new input $\hat{t}$ is obtained using Gaussian Mixture Regression (GMR). Specifically, the probabilistic reference trajectory $\mathcal{G} = \left\{ t_n, \hat{\mu}_n, \hat{\Sigma}_n \right\}_{n=1}^{N}$ can be retrieved by GMR, which encapsulates the distribution of demonstrations.

3.3. Motion/Force Synchronous Kernelized Movement Primitive

GMM can effectively capture the probabilistic characteristics of multiple samples, accommodating both time sequences and multidimensional data inputs. For a given time sequence $\{t_n\}_{n=1}^{N}$ spanning the input space, we can derive its probabilistic reference sequence $\mathscr{G} = \left\{t_n, \hat{\mu}_n, \hat{\Sigma}_n\right\}_{n=1}^{N}$, where the mean and covariance are computed as outlined in (25). This sequence represents the characteristics of the motion and force trajectory of bone-setting demonstrations.

Subsequently, KMP is utilized to learn the probabilistic characteristics and generalize the reference sequence. The distribution of the reference curve $D(t)$ is then expressed in a parameterized form:

$$D(t) = \Theta(t)^{\mathrm{T}}\omega \sim \mathbb{N}(\Theta(t)^{\mathrm{T}}\mu_{\omega}, \Theta(t)^{\mathrm{T}}\Sigma_{\omega}\Theta(t)) \tag{26}$$

where $\Theta(t) = \delta(t)I_{\mathscr{O}}$ is a matrix of $\mathscr{B}$-dimensional basis functions $\delta(t) \in \mathbb{R}^{\mathscr{B}}$ and $\omega \in \mathbb{R}^{\mathscr{B}\mathscr{O}}$ is a weight vector. To formulate KMP, the following objective function is defined:

$$J(\mu_{\omega}, \Sigma_{\omega}) = \sum_{n=1}^{N} D_{KL}(P_p(\mathscr{g}|t_n)||P_r(\mathscr{g}|t_n)) \tag{27}$$

where $P_p(\mathscr{g}|t_n)$ *and* $P_r(\mathscr{g}|t_n)$ are the probabilistic distributions of the parametric and reference trajectories, respectively, given the input t_n. The Kullback–Leibler divergence, denoted D_{KL}, is a measure of the difference between the two distributions.

The choice of the kernel function is the Gaussian function kernel, which can be denoted as $k(\cdot,\cdot)$. The kernel constructs the kernel matrix K as follows:

$$K = \begin{bmatrix} k(t_1,t_1) & k(t_1,t_1) & \cdots & k(t_1,t_1) \\ k(t_2,t_1) & k(t_2,t_2) & \cdots & k(t_2,t_N) \\ \vdots & \vdots & \ddots & \vdots \\ k(t_N,t_1) & k(t_N,t_2) & \cdots & k(t_N,t_N) \end{bmatrix} \tag{28}$$

Similarly, when a new input t^* is given, the kernel matrix k^* can be constructed as follows:

$$k^* = [k(t^*,t_1)\, k(t^*,t_2)] \ \ldots \ k(t^*,t_N)] \tag{29}$$

The kernelized mean expectation of KMP for the new input is then [26,27]:

$$\mu_{\omega}(t^*) = k^*(K + \gamma\Sigma)^{-1}\mu \tag{30}$$

The covariance expectation for the input s^* can be similarly kernelized as

$$\Sigma_{\omega}(t^*) = \frac{N}{\gamma_c}\left(k(t^*,t^*) - k^*(K + \gamma\Sigma)^{-1}, k^{*\mathrm{T}}\right) \tag{31}$$

where γ and γ_c are regularization factors introduced to avoid overfitting the mean and covariance predictions, respectively. And

$$\Sigma = \mathrm{blockdiag}(\hat{\Sigma}_1, \hat{\Sigma}_2, \ \ldots, \hat{\Sigma}_N) \tag{32}$$

$$\mu = \left[\hat{\mu}_1{}^{\mathrm{T}}, \hat{\mu}_2{}^{\mathrm{T}}, \ldots, \hat{\mu}_N^{\mathrm{T}}\right]^{\mathrm{T}} \tag{33}$$

Thus far, KMP is used to perform synchronized imitation learning for bone-setting motion and force trajectories. To enable personalized planning for different cases, its modulation function allows trajectory adaptation through new via-points or target endpoints [26,27]. Hence, we can define a new reference $\widetilde{\mathscr{G}}$ database with V new desired

points, and $\widetilde{\mathcal{G}} = \left\{t_n, \widetilde{\mu}_n, \widetilde{\Sigma}_n\right\}_{v=1}^{V}$. An extended reference database can be defined as $\mathcal{G}^e = \left\{t_i^e, \mu_i^e, \Sigma_i^e\right\}_{i=1}^{N+V}$. Then, the objective function can be rewritten as follows:

$$J_{mod}^e(\mu_\omega, \Sigma_\omega) = \sum_{i=1}^{N+V} D_{KL}(P_p(\mathcal{g}|t_i^e)||P_r(\mathcal{g}|t_i^e)) \tag{34}$$

where $P_p(\mathcal{g}|t_i^e)$ and $P_r(\mathcal{g}|t_i^e)$ are the probabilistic distributions of the parametric and reference trajectories, which are related to the extended reference database. Therefore, we can predict the mean and covariance for new queries by following (30) and (31).

4. Dual-Lyer Hybrid Admittance Control for Dual-Arm Bone-Setting Robot

Building upon the motion–force trajectories of robotic bone-setting obtained in the previous section, this study further investigates dual-arm cooperative control for fracture reduction. To this end, we developed a novel dual-layer hybrid admittance controller comprising an ankle-layer and a robot-layer. This controller ensures safe and effective orthopedic reduction, as illustrated in Figure 5. For clarity, the definitions of variables related to the controller are provided in Table 2.

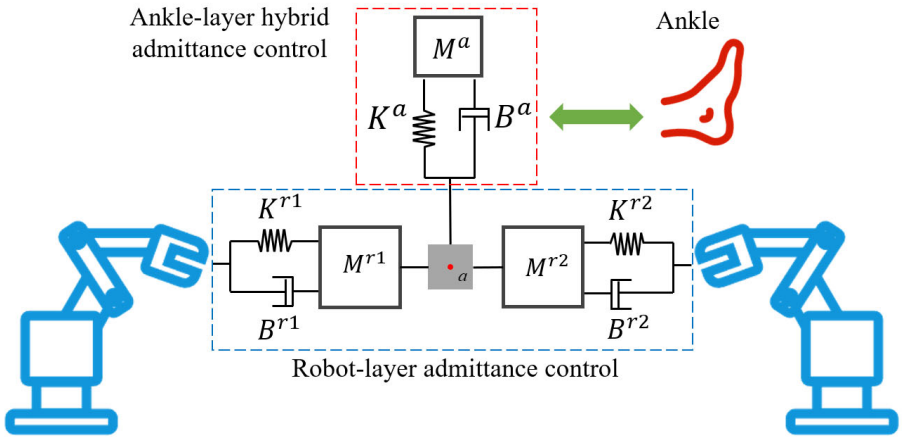

Figure 5. Diagram of dual-layer hybrid admittance control scheme for the bone-setting robot.

4.1. Ankle-Layer Hybrid Admittance Controller

The primary objective of the ankle-layer admittance controller is to enable accurate and non-invasive fracture reduction of the ankle. Guided by TCB experts, we focus on two critical components: the reduction force in translational space and the orientation trajectory in rotational space. In non-invasive scenarios, it is often difficult to measure and reproduce displacement trajectories precisely, particularly for stretching. Therefore, we emphasize defining target force profiles to replicate expert-applied forces and support personalized treatment. In contrast, orientation trajectories are easier to capture, as they reflect the rotational manipulations performed during reduction. Using the ankle frame as the reference coordinate system, expert-applied rotational angles can be quantitatively recorded and incorporated into the learning framework. For example, based on the principle of inverse reduction, the fixation angle after realignment must remain within a specific range to ensure anatomical stability and therapeutic effectiveness.

Table 2. Description of dual-layer hybrid admittance controller.

Symbol	Description
$p_i^a, \dot{p}_i^a, \ddot{p}_i^a$	The real position, velocity, acceleration in Ankle-layer, $i \in \{x, y, z\}$, denote the three dimensions of translational space.
$p_{di}^a, \dot{p}_{di}^a, \ddot{p}_{di}^a$	The expected position, velocity, acceleration in Ankle-layer, $i \in \{x, y, z\}$, denote the three dimensions of rotational space.
$\vartheta_i^a, \dot{\vartheta}_i^a, \ddot{\vartheta}_i^a$	The real angle, angular velocity, angular acceleration in Ankle-layer.
$\vartheta_{di}^a, \dot{\vartheta}_{di}^a, \ddot{\vartheta}_{di}^a$	The expected angle, angular velocity, angular acceleration in Ankle-layer.
$M_{pi}^a,\ B_{pi}^a,\ K_{pi}^a$	The inertia, damp, and stiffness of admittance control in the translational space of Ankle-layer.
$M_{\vartheta i}^a, B_{\vartheta i}^a, K_{\vartheta i}^a$	The inertia, damp, and stiffness of admittance control in the rotational space of Ankle-layer.
$p_i^{ru}, \dot{p}_i^{ru}, \ddot{p}_i^{ru}$	The real position, velocity, acceleration in Robot-layer, $u \in \{1,\ 2\}$, represent left or right robot arm.
$p_{di}^{ru}, \dot{p}_{di}^{ru}, \ddot{p}_{di}^{ru}$	The expected position, velocity, acceleration in Robot-layer.
$\vartheta_i^{ru}, \dot{\vartheta}_i^{ru}, \ddot{\vartheta}_i^{ru}$	The real angle, angular velocity, angular acceleration in Robot-layer.
$\vartheta_{di}^{ru}, \dot{\vartheta}_{di}^{ru}, \ddot{\vartheta}_{di}^{ru}$	The expected angle, angular velocity, angular acceleration in Robot-layer.
$M_{pi}^{ru}, B_{pi}^{ru}, K_{pi}^{pu}$	The inertia, damp, and stiffness of admittance control in the translational space of Robot-layer.
$M_{\vartheta i}^{ru}, B_{\vartheta i}^{ru}, K_{\vartheta i}^{ru}$	The inertia, damp, and stiffness of admittance control in the rotational space of Robot-layer.

Accordingly, inspired by the concept of force/position hybrid control [37,38,62], we adopt force tracking in translational space and trajectory tracking in rotational space. Variable admittance control is used to follow the target force trajectory, while admittance control in the rotational domain enables compliant orientation adjustment. The ankle-layer admittance controller is formulated as follows:

$$\begin{cases} M_{pi}^a\left(\ddot{p}_{di}^a - \ddot{p}_i^a\right) + B_{pi}^a\left(\dot{p}_{di}^a - \dot{p}_i^a\right) + \Delta K_{pi}^a\left(p_{di}^a - p_i^a\right) = \Delta F_{Ei}^a \\ M_{\vartheta i}^a\left(\ddot{\vartheta}_{di}^a - \ddot{\vartheta}_i^a\right) + B_{\vartheta i}^a\left(\dot{\vartheta}_{di}^a - \dot{\vartheta}_i^a\right) + K_{\vartheta i}^a\left(\vartheta_{di}^a - \vartheta_i^a\right) = \Delta M_{Ei}^a \end{cases} \tag{35}$$

where $i \in \{x, y, z\}$ denote the three dimensions of translational or rotational space. The variable $\Delta F_{Ei}^a = F_{Ei}^a - F_{Edi}^a$ represents the difference between the actual external force and the expected external force for the ankle, while $\Delta M_{Ei}^a = M_{Ei}^a - M_{Edi}^a$ denotes the difference between the actual external torque and the expected external torque for the ankle. Here, F_{Edi}^a corresponds to the reduction force trajectory generated by the KMP, and M_{Edi}^a is defined as zero. ΔK_{pi}^a represents the variable stiffness coefficient. To be specific, the ankle-layer admittance controller in the translational space is adjusted to

$$M_{pi}^a\left(\ddot{p}_{di}^a - \ddot{p}_i^a\right) + B_{pi}^a\left(\dot{p}_{di}^a - \dot{p}_i^a\right) + \Delta K_{pi}^a(p_{di}^a - p_i^a) = \Delta F_{Ei}^a \tag{36}$$

Defining $\Delta p^a = p_d^a - p^a$ and $\Delta \vartheta^a = \vartheta_d^a - \vartheta^a$ yields

$$M_p^a\left(\Delta\ddot{p}^a\right) + B_p^a\left(\Delta\dot{p}^a\right) + \Delta K_p^a(\Delta p^a) = \Delta F_E^a \tag{37}$$

Based on inspiration from reference [56], a novel variable stiffness control law is designed as follows:

$$\begin{cases} \Delta K_p^a = \frac{\varphi(t)}{\Delta p^a(t)} \\ \varphi(t) = \varphi(t-T) + \rho \frac{\Delta F_E^a(t-T)}{B_p^a} \end{cases} \tag{38}$$

where T denotes the sampling period of the system, and ρ denotes a positive gain of force error.

According to reference [56], the stability and convergence of the control law have been verified. The range of ρ is:

$$0 < \rho < \frac{B_p^a T}{B_p^a T + M_p^a} \tag{39}$$

Experimental results indicate that larger values of ρ lead to more pronounced force oscillations, whereas smaller values help suppress these fluctuations. To enhance system stability and adaptability during bone-setting procedures, and to accommodate the biomechanical variability of the ankle, real-time adjustment of ρ is essential. Fuzzy control strategy offers robust performance even under uncertain system dynamics and nonlinear interactions, making it particularly well suited for complex environments such as medical robotics [44,45,63]. Hence, we propose a novel Adaptive Fuzzy Variable Admittance Controller (AFVAC) to improve real-time flexibility and control accuracy in orthopedic applications.

This study takes the error force ΔF_{Ei}^a and the rate of change of force error $\Delta \dot{F}_{Ei}^a$ as inputs to the fuzzy controller, and gives the following basic domain of input–output based on actual situations:

$$\Delta F_E^a \in [-15, 15]; \Delta \dot{F}_{Ei}^a \in [-15, 15]; u_\rho \in [0, \rho_{max}] \tag{40}$$

According to the given range, set seven grades: positive big (PB), positive medium (PM), positive small (PS), zero (ZO), negative big (NB), negative medium (NM) and negative small (NS). The fuzzy input subset and fuzzy output subset are both set as:

$$\{NB,\ NM,\ NS,\ ZO,\ PS,\ PM,\ PB\} \tag{41}$$

In fuzzy control strategy, membership functions define the degree to which input variables belong to fuzzy sets and serve as the foundation for fuzzy inference and decision making. Among various forms, triangular membership functions are widely used for their simplicity and computational efficiency. Accordingly, this study adopts triangular membership functions for both input variables, as illustrated in Figure 6a. The fuzzy rule base establishes the relationship between inputs and output, and is designed based on expert knowledge and empirical observations. With seven fuzzy subsets assigned to each input variable, a total of 49 fuzzy rules are generated. The complete set of control rules is provided in Table 3, and the corresponding control surface is shown in Figure 6b.

Using the Mamdani fuzzy reasoning method to obtain the output membership degrees of different fuzzy sets from the rule table, Table 3 can be represented as follows. If $\Delta F_E^a = A_i$ and $\Delta \dot{F}_E^a = B_j$ $(j = 1, 2, \ldots, 7)$, then $u_\rho = C_k(A_i, B_j)$ $(k = 1, 2, \ldots, 49)$, Among them, A_i and B_i represent the *i-th* or *j-th* fuzzy rules corresponding to ΔF_E^a and $\Delta \dot{F}_E^a$, while C_k represents the fuzzy output of A_i and B_j in the *k-th* fuzzy rule.

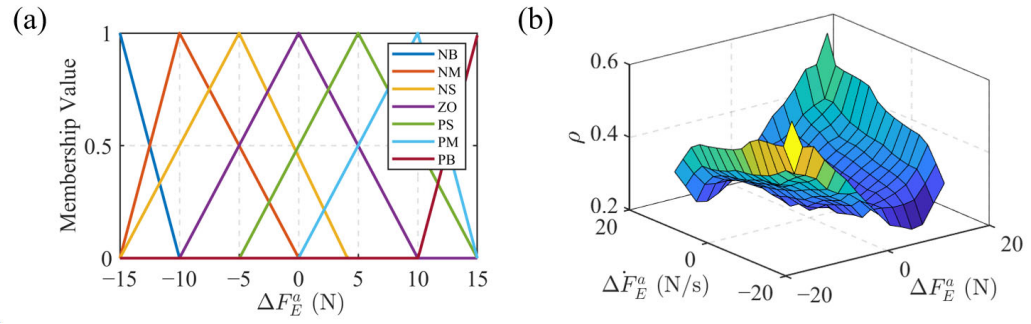

Figure 6. Fuzzy control strategy. (**a**) Schematic diagram of membership function. (**b**) Surface viewer of fuzzy control.

Table 3. Fuzzy control rule table.

E \ EC	NB	NM	NS	ZO	PS	PM	PB
NB	PB	PB	PM	PM	PS	PS	ZO
NM	PB	PM	PM	PS	PS	ZO	NS
NS	PM	PS	ZO	NS	NS	NM	NM
ZO	ZO	NS	NM	NP	NM	NS	ZO
PS	NM	NM	NS	NS	ZO	PS	PM
PM	NS	ZO	PS	PS	PM	PM	PB
PB	ZO	PS	PS	PM	PM	PB	PB

Choose the center of gravity defuzzification method to defuzzify the output fuzzy set, that is,

$$\rho = \frac{\sum_{k=1}^{K} C_k\left(A_i, B_j\right) * \Delta F_E^a(i) * \Delta F_{Ec}^a(j)}{\sum_{k=1}^{N} \Delta F_E^a(i) * \Delta F_{Ec}^a(j)} \tag{42}$$

where K represents the number of fuzzy rules; $C_k\left(A_i, B_j\right)$ is the membership grade of the *k-th* fuzzy output; $\Delta F_E^a(i)$ and $\Delta \dot{F}_E^a(j)$ are the input value corresponding to the current membership degree. By adjusting the stiffness parameter, admittance control can effectively track the traction tension force, and the stability of its orthopedic process can be improved by adding fuzzy control.

4.2. Robot-Layer Admittance Controller

The motion trajectories of both robotic arms are computed based on closed-chain kinematic constraints to ensure accurate ankle reduction. However, in practical settings, deviations often occur between the theoretical constraints modeled in SolidWorks 2023 and the actual constraints, due to machining and assembly errors in the end-effectors. In tightly coordinated control scenarios, even minor trajectory deviations can generate significant internal forces, which may damage the robotic arms and compromise the safety and effectiveness of bone-setting procedures. To address this issue, we introduce a robot-layer admittance controller that enables real-time correction of dual-arm trajectories. This controller compensates for disturbances caused by constraint deviations, thereby improving both control stability and operational safety. The mathematical formulation is presented below:

$$\begin{cases} M_{pi}^{ru}\left(\ddot{p}_{di}^{ru} - \ddot{p}_i^{ru}\right) + B_{pi}^{ru}\left(\dot{p}_{di}^{ru} - \dot{p}_i^{ru}\right) + K_{pi}^{ru}\left(p_{di}^{ru} - p_i^{ru}\right) = \Delta F_{Ii}^{ru} \\ M_{\vartheta i}^{ru}\left(\ddot{\vartheta}_{di}^{ru} - \ddot{\vartheta}_i^{ru}\right) + B_{\vartheta i}^{ru}\left(\dot{\vartheta}_{di}^{ru} - \dot{\vartheta}_i^{ru}\right) + K_{\vartheta i}^{ru}\left(\vartheta_{di}^{ru} - \vartheta_i^{ru}\right) = \Delta M_{Ii}^{ru} \end{cases} \tag{43}$$

where $\Delta F_{Ii}^{ru} = F_{Ii}^{ru} - F_{Idi}^{ru}$ represents the difference between the actual internal force and the expected internal force of the robotic arm. Similarly, $\Delta M_{Ii}^{ru} = M_{Ii}^{ru} - M_{Idi}^{ru}$ denotes the difference between the actual internal torque and the expected internal torque for the robotic arm. In this context, both F_{Idi}^{ru} and M_{Idi}^{ru} are set to zero.

Based on the above description, we summarized and drew the framework diagram of closed reduction skill learning and dual-layer hybrid admittance control for a dual-arm bone-setting robot, which can be shown in Figure 7.

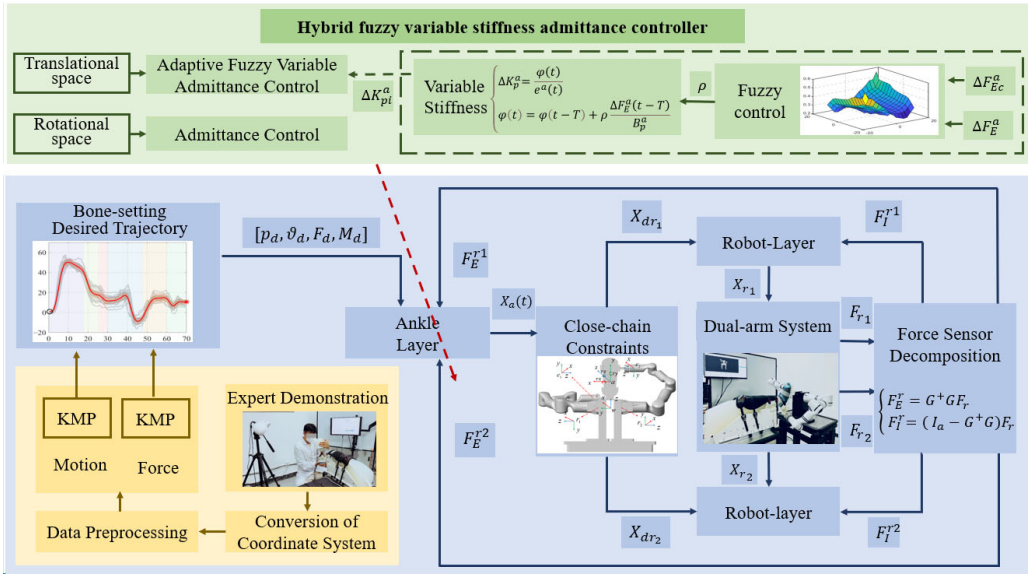

Figure 7. The framework of closed reduction skill learning and dual-layer hybrid admittance control for a dual-arm bone-setting robot.

5. Experiment and Evaluation

5.1. Experiment Setup

Figure 2 shows the dual-arm bone-setting robotic system and its key components for human–robot interaction [41]. The system features two 7-DoF RM-75B robotic arms (RealMan, Beijing, China), capable of performing complex six-dimensional movements. Each robot arm has a repeatability of 0.05mm and a rated payload of 5 kg. A six-axis force/torque sensor is installed at the end-effector of each arm to enable accurate force measurement during bone-setting. Operating at 50 Hz, these sensors provide real-time feedback for forces and torques, supporting the implementation of admittance control.

To evaluate the effectiveness of the proposed reduction method, we applied KMP and DMP to learn both motion and force trajectories involved in a representative ankle fracture reduction task. Specifically, we selected a supination-type fracture case, a common injury characterized by rotational displacement of the talus and fibula. Based on the learned model, we conducted a series of evaluations, including trajectory reproduction, personalized adaptation, and disturbance rejection analysis. To ensure consistency, a Gaussian Mixture Model (GMM) with 20 components was used for trajectory modeling, with a demonstration duration of 70 s and a trajectory length of N = 140. For quantitative evaluation, we employed three widely used similarity metrics: Dynamic Time Warping Distance (DTWD), Fréchet Distance (FD), and Root Mean Square Error (RMSE). Among them, DTWD measures temporal alignment between trajectories, FD captures spatial similarity, and RMSE quantifies the point-wise deviation between the reproduced and reference trajectories. Collectively, these metrics provide a comprehensive assessment of the imitation learning performance. Lower values across all three metrics indicate higher fidelity and more accurate reproduction of expert demonstrations.

To comprehensively evaluate the effectiveness of the proposed hybrid admittance controller, five representative controllers in the translational space of the ankle layer were selected for comparative experiments. These include a Constant Admittance Control (CAC) strategy and four Adaptive Variable Admittance Control (AVAC) strategies with different modulation coefficients [56]. The parameter settings for the controller are listed in Table 4. For both the rotational space of the ankle layer and the robot layer, identical admittance parameters were applied across all experiments. Specifically, the admittance parameters for the rotational space of the ankle layer are $M^a_{\vartheta i} = 0.6\ \mathrm{kg{\cdot}m^2}$, $B^a_{\vartheta i} = 30\ \mathrm{N{\cdot}m{\cdot}s/rad}$, $K^a_{\vartheta i} = 800\ \mathrm{N{\cdot}m/rad}$, and those for the robot layer are $M^{ru}_{pi} = 0.6\ \mathrm{kg}$, $B^{ru}_{pi} = 35\ \mathrm{N{\cdot}\frac{s}{m}}$, $K^{ru}_{pi} = 3000\ \mathrm{N/m}$, $M^{ru}_{\vartheta i} = 0.6\ \mathrm{kg{\cdot}m^2}$, $B^{ru}_{\vartheta i} = 30\ \mathrm{N{\cdot}m{\cdot}s/rad}$ and $K^{ru}_{\vartheta i} = 800\ \mathrm{N{\cdot}m/rad}$. It should be noted that these parameters were selected based on empirical tuning and the adjustment principles reported in previous studies [64,65], taking into account the dynamic characteristics of the robot and ensuring stable and responsive control performance.

Table 4. Experimental parameter for Ankle-layer.

Controller		Parameter Value
Ankle-layer	CAC	$M^a_{pi} = 0.9\ \mathrm{kg},\ B^a_{pi} = 30\ \mathrm{N{\cdot}s/m},\ K^a_{pi} = 1500\ \mathrm{N/m}$
	AVAC-0.05	$M^a_{pi} = 1.6\ \mathrm{kg},\ B^a_{pi} = 280\ \mathrm{N{\cdot}s/m},\ \rho = 0.05$
	AVAC-0.2	$M^a_{pi} = 1.6\ \mathrm{kg},\ B^a_{pi} = 280\ \mathrm{N{\cdot}s/m},\ \rho = 0.2$
	AVAC-0.4	$M^a_{pi} = 1.6\ \mathrm{kg},\ B^a_{pi} = 280\ \mathrm{N{\cdot}s/m},\ \rho = 0.4$
	AVAC-0.6	$M^a_{pi} = 1.6\ \mathrm{kg},\ B^a_{pi} = 280\ \mathrm{N{\cdot}s/m},\ \rho = 0.6$
	AFVAC	$M^a_{pi} = 1.6\ \mathrm{kg},\ B^a_{pi} = 280\ \mathrm{N{\cdot}s/m},\ \rho \in [0,\ 0.78]$

Moreover, we utilized several performance metrics to assess the accuracy and robustness of the learned trajectories. These metrics include RMSE (Root Mean Square Error), MAE (Mean Absolute Error), SD (Standard Deviation), IAE (Integral of Absolute Error), and MAX (Maximum Error). These metrics provide a multidimensional assessment of the reduction method's performance, offering critical insights into its application for ankle fracture reduction. Through this comprehensive analysis, we can better understand the method's precision, consistency, and robustness in replicating target movements.

5.2. Trajectory Reproduction Experiment

In this section, we applied KMP to obtain synchronized motion and force trajectories by learning twelve reduction demonstrations from Section 3.1. Notably, the parameters of KMP are obtained by a heuristic optimization algorithm. One demonstration was chosen as a reference, with its start and end points set as constraints to guide the KMP algorithm in generating new target trajectories for motion and force, intended for the admittance controller. Figure 8 shows the results of the reproduction test. As shown in Figure 8e, DMP deviates from the demonstrated trajectory, whereas KMP not only preserves trajectory similarity but also ensures superior smoothness. The KMP-generated trajectories align closely with the demonstrations, adhering to the start and end constraints. Compared to DMP, the KMP-generated trajectories more accurately adhere to the demonstration data, underscoring their superior capability in replicating expert actions. It is a crucial requirement for precise trajectory planning in personalized treatments. Quantitative results in Table 5 further support this finding. For DTWD, the primary similarity metric, the KMP-generated trajectories for translation, orientation, force, and torque achieved values of 41.441 mm, 88.338 mm, 110.060 mm, and 9.907 mm, respectively, compared to the expert trajectories. Moreover, KMP consistently outperforms DMP across metrics, including DTWD, FD, and RMSE, demonstrating higher accuracy in replicating multiple expert demonstrations. Over-

all, these results confirm that KMP not only meets basic trajectory generation requirements but also closely mirrors reduction maneuvers from the TCB experts.

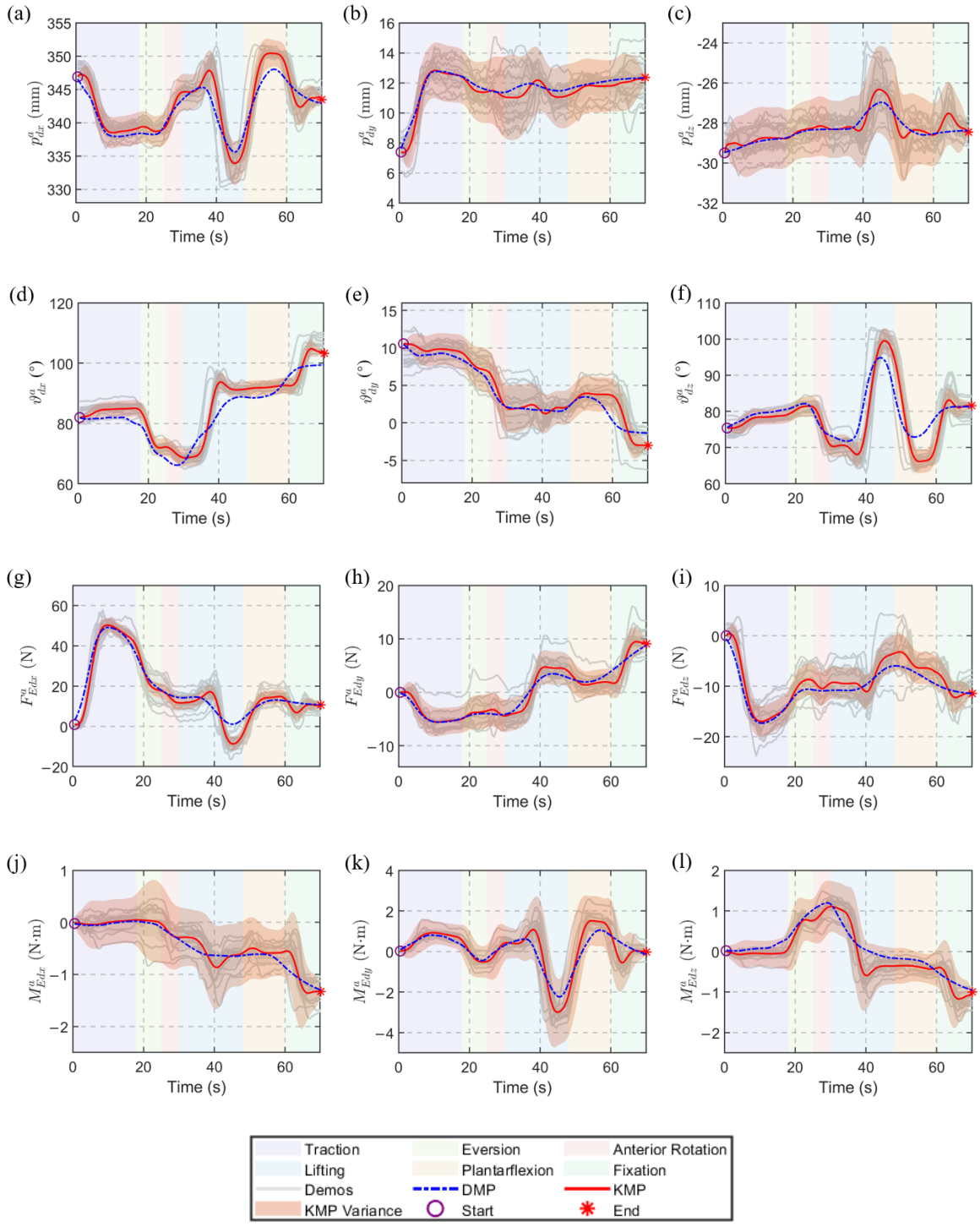

Figure 8. Reproduction trajectories based on KMP. The solid gray lines in the figure represent the original twelve demo curves, respectively, representing the six action processes of bone reset from left to right, corresponding to the six acquisition actions in Figure 5. The blue dashed line represents the reference trajectory generated by DMP, which is used for comparison, the red implementation represents the reset trajectory generated by KMP, and the red band represents the variance band of the KMP trajectory. (**a**–**c**) Expected position along the X, Y, and Z axes. (**d**–**f**) Expected orientation angle around the RX, RY, and RZ axes. (**g**–**i**) Expected force along the X, Y, and Z axes. (**j**–**l**) Expected torque around the RX, RY, and RZ axes.

Table 5. Reproduction test results for KMP and DMP.

	KMP			DMP		
	DTWD	**FD**	**MSE**	**DTWD**	**FD**	**MSE**
Position (mm)	41.443	3.0892	1.7654	295.31	30.324	2.1402
Orientation (°)	88.338	6.4624	7.5686	834.17	69.045	18.027
Force (N)	110.06	8.6662	11.532	764.55	72.958	27.974
Torque (N·m)	9.9070	0.7509	0.0107	73.319	7.6521	0.1506

We further evaluated the performance of the admittance controller using the dual-arm bone-setting robotic platform and the motion–force trajectories obtained in Figure 8. In the experiments, the robot manipulated a silicone ankle prosthesis with unknown stiffness and geometric uncertainties. The controller parameters are listed in Table 4, and the full bone-setting procedure is illustrated in Figure 9. A comparison between Figure 9 and the demonstration acquisition process shown in Figure 4 reveals that the robotic bone-setting process exhibits strong consistency with expert demonstrations and demonstrates human-like characteristics. Notably, during the initial phase (0–10 s), the robot performed stretching and traction maneuvers, accurately tracking the expert-level three-dimensional reduction force profiles in translational space. In subsequent phases, the robot continued to track time-varying desired forces with good precision under compliant contact conditions. Regarding orientation tracking, the use of a constant admittance control strategy led to more stable performance. The evolution of relevant control parameters over time is shown in Figure 10.

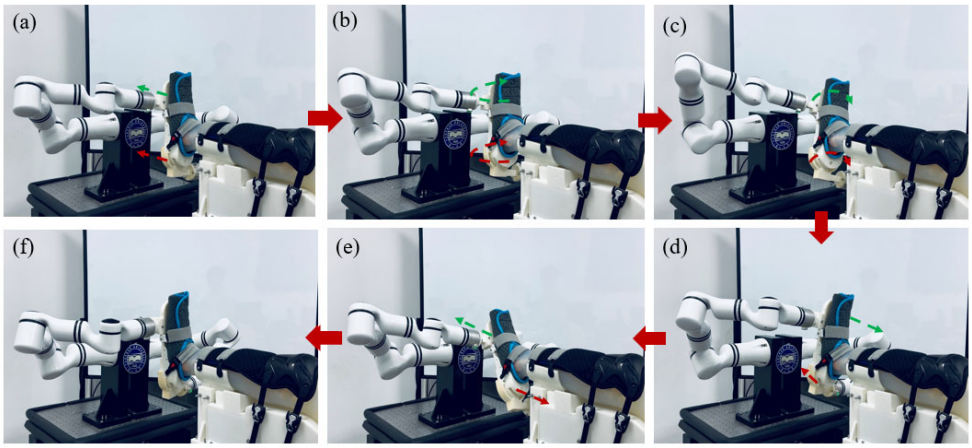

Figure 9. Robot bone-setting process. (**a**) Traction. (**b**) Eversion. (**c**) Anterior Rotation. (**d**) Lifting. (**e**) Plantarflexion. (**f**) Fixation.

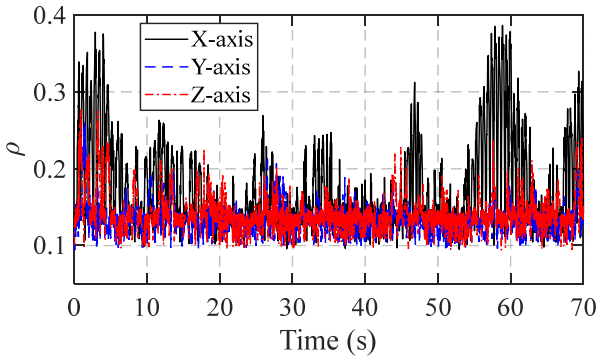

Figure 10. The curves for variable parameters ρ.

In the comparative experiments, we selected five different controllers to evaluate their performance in external force tracking. Figure 11 compares the force and orientation tracking errors among six controllers, offering insights into their relative performance. The results indicate that, for the tracking tasks involving time-varying, multi-axis reduction forces, the fixed-parameter admittance controller exhibited poor convergence due to its lack of adaptive impedance adjustment, leading to poor force tracking performance. In contrast, compared to other adaptive variable admittance controllers, the proposed method not only maintained excellent orientation tracking but also demonstrated superior accuracy and faster convergence in force tracking during reduction. For instance, as shown in Figure 11a, during the stretching operation between 0 s and 10 s, the proposed controller exhibited a notably faster convergence rate. Specifically, the RMSE for force tracking along the X-axis was 2.718 mm using the proposed controller, whereas the RMSE values for the other five controllers were 34.009 mm, 5.465 mm, 5.556 mm, 8.280 mm, and 11.392 mm, respectively. Figure 11d–e demonstrate that the robot achieved precise tracking of the reduction orientation trajectory, with angular errors remaining steadily within $\pm 0.3°$, indicating high control accuracy.

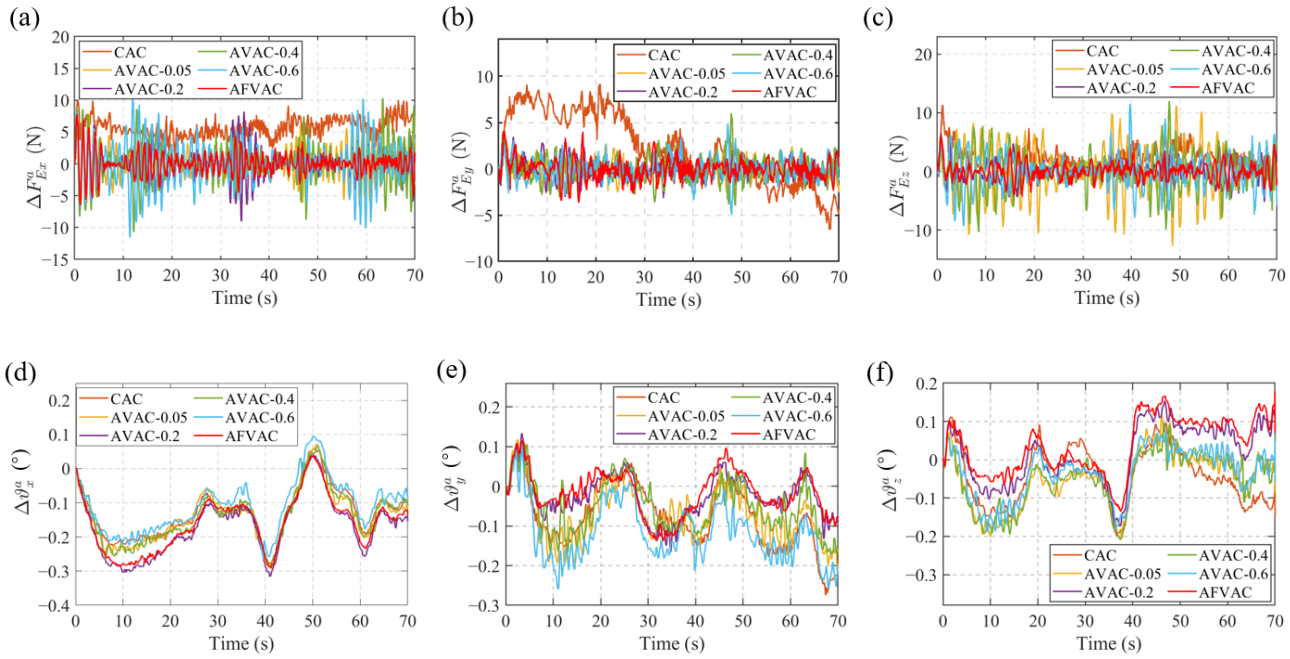

Figure 11. The reduction force and orientation error under the control of different controllers. (**a**) Force tracking error in the X-axis direction. (**b**) Force tracking error in the Y-axis direction. (**c**) Force tracking error in the Z-axis direction. (**d**) Angle tracking error around the RX axis. (**e**) Angle tracking error around the RY axis. (**f**) Angle tracking error around the RZ axis.

Figure 12 presents a comparative evaluation of controller performance across five metrics using a radar chart. In this chart, a smaller enclosed area indicates better force-tracking accuracy. The proposed AFVAC controller achieved the smallest enclosed area, demonstrating superior overall performance. While the AVAC controller with $\rho = 0.05$ exhibited comparable results, it was less effective than AFVAC in tracking force along the X-axis. Specifically, AFVAC reduced the root mean square error (RMSE) in X-axis force tracking by 50.35% compared to AVAC.

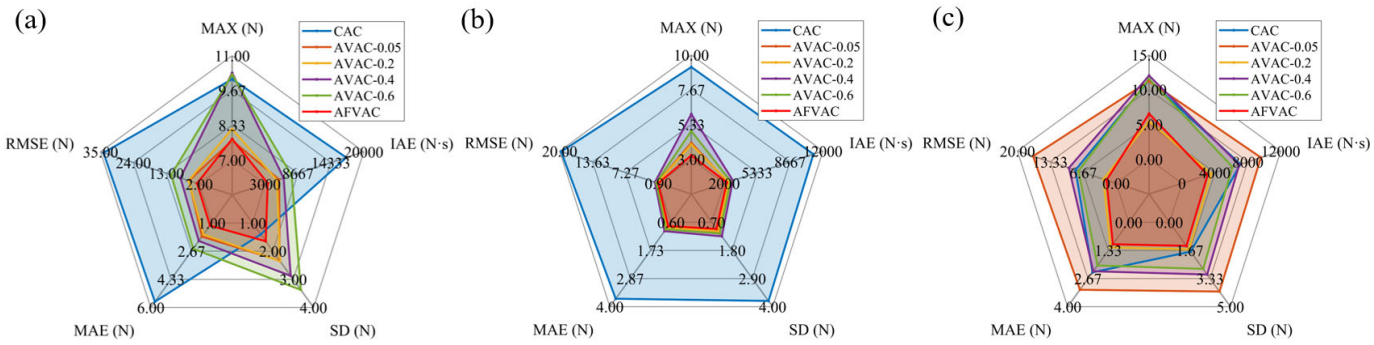

Figure 12. Comparison of the reduction force-tracking performance. (**a**) Force in the X-axis direction. (**b**) Force in the Y-axis direction. (**c**) Force in the Z-axis direction.

5.3. Trajectory Generalization Experiment

To further validate the proposed framework's ability to meet the personalized requirements in orthopedic settings, we conducted a via-point generalization test for the reduction trajectory. Under the guidance of professional TCB experts and based on individual patient characteristics, we specified several critical via-points for the reduction trajectory to individualize the reduction plan. Specifically, for the translational force trajectory, we increased the peak traction force and extended its duration. The via-points were defined as $(12,\ 60)$ and $(15,\ 60)$ for the X-axis, $(12, -5)$ and $(15, -5)$ for the Y-axis, and $(12, -15)$ and $(15, -15)$ for the Z-axis as well. For the reduction orientation trajectory, the maximum dorsiflexion (upward foot bending) and plantarflexion (downward foot pointing) angles were manually defined to optimize joint alignment and improve the reduction outcome. Via-points for orientation were defined as $(45,\ 90)$, $(50,\ 90)$, $(55,\ 90)$, and $(60,\ 90)$ for the RX-axis; $(45,\ 0)$, $(50,\ 5)$, $(55,\ 5)$, and $(60,\ 5)$ for the RY-axis; and $(45,\ 10)$, $(50,\ 98)$, $(55,\ 77)$, and $(60,\ 70)$ for the RZ-axis. Figure 13 presents the trajectory generated by the KMP algorithm, which is evaluated based on defined via-points. Specifically, Figure 13a shows that the proposed algorithm accurately regulates the maximum traction force to the target value of 60 N, highlighting its controllability and suitability for patient-specific orthopedic interventions. Moreover, the mean error for the generated trajectory at key points was 0.135 N for the reduction force and 0.063° for the orientation. Compared to expert demonstration trajectories, the generated reduction force and orientation trajectories achieved DTWD of 127.55 N and 105.03 N, respectively, demonstrating effective trajectory imitation.

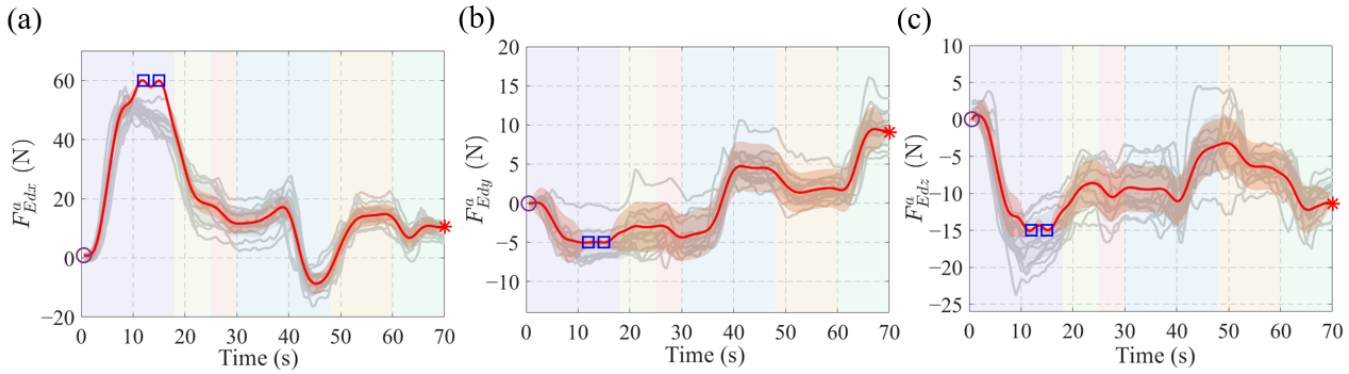

Figure 13. *Cont.*

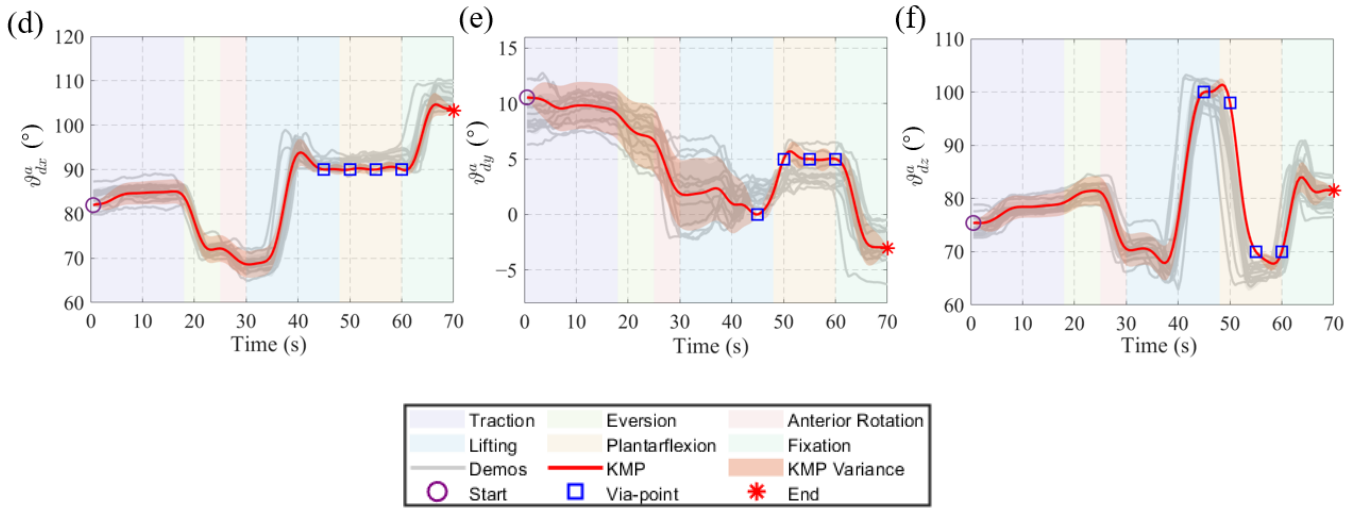

Figure 13. Personalized trajectories based on KMP. The solid gray lines in the figure represent the original twelve demo curves, respectively, representing the six action processes of bone reset from left to right, corresponding to the six acquisition actions in Figure 5. The red implementation represents the personalized trajectories generated by KMP, and the red band represents the variance band of the KMP trajectory. (**a**) Expected force in the X-axis direction. (**b**) Expected force in the Y-axis direction. (**c**) Expected force in the Z-axis direction. (**d**) Expected angle around the RX axis. (**e**) Expected angle around the RY axis. (**f**) Expected angle around the RZ axis.

Subsequently, the proposed controller was applied to track the desired reduction trajectory. Figure 14 illustrates the tracking errors for the generated reduction force and orientation. For force tracking in Figure 14a, the controller maintained the errors within the range of −5 N to 7.5 N, with RMSE values of 1.6414 N, 1.1194 N, and 1.5445 N along the X, Y and Z axes. For orientation tracking in Figure 14b, errors ranged from −0.28° to 0.12°, with RMSE values of 0.0024°, 0.0019°, and 0.0018° on the corresponding axes. These results demonstrate that the proposed framework effectively meets the personalized demands of bone-setting procedures and accurately replicates expert bone-setting skill.

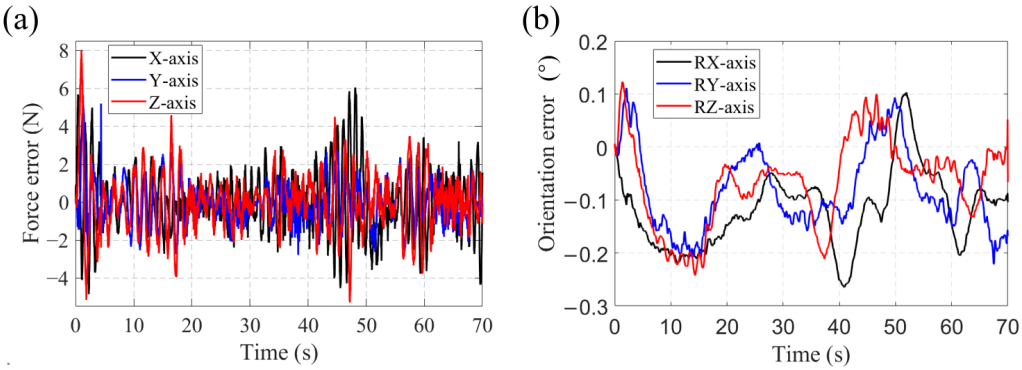

Figure 14. Result of personalized trajectory generalization experiment. (**a**) The reduction force error. (**b**) The reduction orientation error.

In summary, the KMP-based personalized trajectory generation, combined with the AFVAC control strategy, enables precise tracking of transitional points and achieves high accuracy in both translational force and orientation control. It also shows robust performance in controlling both translational forces and orientation angles. This offers robust support for robotic assistance in reduction surgeries, particularly in scenarios requiring highly personalized and precise operations, underscoring its significant clinical value.

5.4. Disturbance Experiment

To further assess the robustness of the proposed framework under personalized conditions, a disturbance experiment was conducted. In this section, we consider the possibility of physiological phenomena, such as muscle spasms, occurring during TCB, which can introduce unexpected disturbances. To evaluate the controller's disturbance rejection capabilities, we conducted robotic bone-setting experiments based on the personalized trajectories obtained in the previous section. We introduced three intentional disturbances at approximately 3 s, 18 s, and 44 s. Figure 15 illustrates the tracking performance of the reduction force and the corresponding error under these disturbance conditions. Although the external disturbances caused deviations in the force trajectory, the system demonstrated significant compliance, which is essential for preventing iatrogenic injuries and ensuring the safety of the bone-setting process. It highlights the framework's clinical relevance. Additionally, the system exhibited great disturbance rejection capabilities, as the controller quickly and stably returned to the target force trajectory after each disturbance. This demonstrates good convergence and control stability.

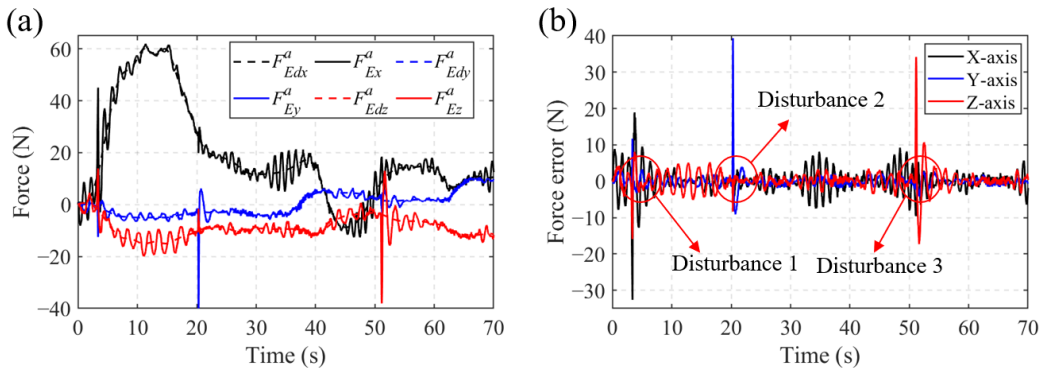

Figure 15. Result of disturbance experiment. (**a**) The reduction forces. (**b**) The reduction force error.

6. Discussion

This study presents a dual-arm robotic system designed to learn and replicate Traditional Chinese Bone-setting (TCB) techniques through a non-invasive, learning-based and compliant framework. A comparison with related methods is presented in Table 6, and the anatomical axis refers to the natural alignment line between the tibia and the talus. Compared to other non-invasive closed reduction systems [24,66], the proposed approach demonstrates superior payload capacity over single-arm configurations and offers a larger orientation workspace than parallel mechanisms, indicating strong overall performance. These features make the system a promising solution for closed reduction procedures, particularly for ankle and distal radioulnar joint fractures. By replicating expert techniques, it improves procedural consistency, reduces clinician workload, and supports less experienced operators. This is particularly valuable in resource-constrained environments where orthopedic expertise and advanced surgical resources may be limited. Ultimately, the proposed system contributes to the democratization of fracture care by enhancing the accessibility, safety, and standardization of manual reduction procedures.

Despite encouraging results, the proposed dual-arm robotic system for closed reduction still faces several limitations that must be addressed prior to broader clinical translation. First, the current design is specifically tailored for ankle fracture reduction and lacks the flexibility to accommodate other anatomical regions, such as the distal radius. This limitation primarily arises from the task-specific bone–robot connection mechanism, which has not yet been generalized to account for the morphological variability across different body parts. Second, although the system effectively learns and replicates expert-like force–motion tra-

jectories using demonstration-based learning, it lacks integrated biomechanical modeling to validate and refine these trajectories. The absence of an integrated musculoskeletal model limits the system's ability to consider tissue mechanics, joint constraints, and bone alignment dynamics throughout the reduction process. Third, the system currently operates in an open-loop configuration without intraoperative imaging integration. The lack of real-time feedback from modalities such as fluoroscopy or X-ray imaging restricts its ability to adapt to anatomical changes during bone-setting, potentially affecting manipulation accuracy and patient safety. Finally, validation experiments have been confined to laboratory environments using silicone limb models. Cadaveric and human subject trials have not yet been conducted, representing a critical next step in evaluating the system's safety, robustness, and clinical feasibility under realistic surgical conditions.

Table 6. Comparison of our work with the state of the art.

	Zha [24]	**Bian [32]**	**Tang [67]**	**Zhu [66]**	**Ours**
Structure type	Single-arm	Single-arm	Parallel	Parallel	Dual-arm
Non-invasive	√	×	×	√	√
Capacity	<50 N	<70 N	>200 N	>200 N	70–200 N
Ultimate angle (Anatomical axis; other two)	>60°; >60°	–	<20°; <20°	–	>60°; >40°
Imitation learning planning	×	√	×	×	√
Compliance control	×	×	×	×	√

7. Conclusions and Future Work

To support the inheritance of Traditional Chinese Bone-setting (TCB) techniques, this paper presents a dual-arm robotic framework for closed reduction skill learning and coordinated control, focusing on ankle fractures. The robot's mechanical design and closed-chain kinematics were analyzed, including force decomposition. A globally optimal reparameterization algorithm and an extended KMP framework were introduced for synchronized motion–force learning. The framework integrates expert-defined via-points to enable personalized adaptation. A dual-layer hybrid variable admittance controller was also developed to ensure compliant control under closed-chain constraints, achieving accurate trajectory and force tracking for safe and effective reduction. Experimental results show that the proposed method successfully replicates expert reduction maneuvers, with DTWD for position and orientation trajectories of 41.443 mm and 88.338 mm, respectively, and DTWD values for force and torque of 110.06 N and 9.907 N. The adaptive fuzzy variable admittance controller implemented at the ankle layer outperformed fixed and conventional adaptive impedance strategies, particularly in X-axis force tracking. Specifically, the RMSE was 2.718 mm for the proposed controller, compared to 34.009 mm, 5.465 mm, 5.556 mm, 8.280 mm, and 11.392 mm for the alternatives. In trajectory personalization experiments, the proposed control framework successfully met the individual requirements specified by the physicians, including maximum stretching force, maximum terminal angle, and maximum plantarflexion angle, while ensuring accurate tracking of the reduction force and position trajectories. Specifically, the RMSE values for force tracking were 1.6414 N, 1.1494 N, and 1.5545 N, and the values for orientation tracking were 0.0024°, 0.0019°, and 0.0018°, respectively. Under disturbance conditions, the proposed controller exhibited great compliance and control stability. Overall, the results indicate that the proposed framework effectively transfers expert bone-setting skills and force feedback, while meeting the individualized and safety requirements of bone-setting procedures. Moreover, the control framework shows strong adaptability and robustness in responding to sudden disturbances, demonstrating high levels of human-like characteristics.

Future work will focus on improving the medical applicability of the bone-setting robot by designing flexible and non-invasive bone–robot connection mechanisms that can support different anatomical regions. Moreover, biomechanical modeling tools such as OpenSim will be integrated to enable personalized optimization and feasibility verification of trajectories based on individual anatomical characteristics. To improve intraoperative adaptability and safety, imaging modalities like X-ray or fluoroscopy will be combined with deep learning-based navigation algorithms, allowing real-time trajectory adjustment during manipulation. Finally, experimental protocols are under development, and ethical approvals are currently underway for cadaveric and human subject trials. These efforts aim to facilitate the comprehensive clinical validation of the proposed system.

Author Contributions: Conceptualization, G.W.; methodology, Z.T.; validation, Y.Y. and X.S.; investigation, J.Z. and X.S.; data curation, Z.T.; writing—original draft preparation, Z.T.; writing—review and editing, G.W. and H.Y.; visualization, Z.T. and J.Z.; supervision, G.W. and Y.Z.; project administration, G.W. and Y.Z.; funding acquisition, G.W. All authors have read and agreed to the published version of the manuscript.

Funding: This work was supported by the National High-Level Innovative Talent Research Foundation of Hebei Province (No. 2021HBQZYCXY003).

Data Availability Statement: The original contributions presented in this study are included in the article. Further inquiries can be directed to the corresponding author.

Acknowledgments: The authors would like to thank the anonymous reviewers for the insightful comments and valuable suggestions.

Conflicts of Interest: The authors declare no conflicts of interest.

References

1. Zhong, F.; Liu, Y.H. Integrated planning and control of robotic surgical instruments for task autonomy. *Int. J. Robot. Res.* **2023**, *42*, 504–536. [CrossRef]
2. Marcus, H.J.; Ramirez, P.T.; Khan, D.Z. The IDEAL framework for surgical robotics: Development, comparative evaluation and long-term monitoring. *Nat. Med.* **2024**, *30*, 61–75. [CrossRef] [PubMed]
3. Liu, T.; Wang, J.; Wong, S.; Razjigaev, A. A Review on the Form and Complexity of Human–Robot Interaction in the Evolution of Autonomous Surgery. *Adv. Intell. Syst.* **2024**, *6*, 2400197. [CrossRef]
4. Zhao, T.; Zhang, Y.; Yuan, J.; Xu, S.; Zhang, J.; Wen, G.; Hu, X.; Yin, H. Modified Dynamic Movement Primitive-Based Closed Ankle Reduction Technique Learning and Variable Impedance Control for a Redundant Parallel Bone-Setting Robot. *Machines* **2025**, *13*, 145. [CrossRef]
5. Cao, C.; Cao, T. Analysis of the influence of traditional bone setting and loosening manipulation of Traditional Chinese Medicine on sports rehabilitation after ankle operation. *J. Mod. Med.* **2023**, *5*, 4. [CrossRef]
6. Zha, Q.; Xu, Z.; Yang, H.; Zhang, G.; Cai, X.; Zhang, W.; Liu, Y.; Shen, X.; Li, Y. Development of a robot-assisted reduction and rehabilitation system for distal radius fractures. *Front. Bioeng. Biotechnol.* **2024**, *11*, 1342229. [CrossRef]
7. Lawson, K.A.; Ayala, A.E.; Morin, M.L.; Latt, L.D.; Wild, J.R. Republication of "Ankle fracture-dislocations: A review". *Foot Ankle Orthop.* **2023**, *8*, 24730114231195058. [CrossRef]
8. Payne, R.; Kinmont, J.C.; Moalypour, S.M. Initial management of closed fracture-dislocations of the ankle. *Ann. Roy. Coll. Surg.* **2004**, *86*, 177–181. [CrossRef]
9. Li, J.; Cui, R.; Su, P.; Ma, L.; Sun, H. A computer-assisted preoperative path planning method for the parallel orthopedic robot. *Machines* **2022**, *10*, 480. [CrossRef]
10. Pan, M.; Chen, Y.; Li, Z.; Liao, X.; Deng, Y.; Bian, G.B. Autonomous path planning for robot-assisted pelvic fracture closed reduction with collision avoidance. *Int. J. Med. Robot. Comput. Assist. Surg.* **2023**, *19*, e2483. [CrossRef]
11. Huang, Y.-L.; Xu, D.; Tan, M. On imitation learning of robot movement trajectories: A survey. *Acta Autom. Sin.* **2022**, *48*, 315–334.
12. Cui, J.; Trinkle, J. Toward next-generation learned robot manipulation. *Sci. Robot.* **2021**, *6*, eabd9461. [CrossRef]
13. Correia, A.; Alexandre, L.A. A survey of demonstration learning. *Robot. Auton. Syst.* **2024**, *182*, 104812. [CrossRef]
14. Pérez-Dattari, R.; Della Santina, C.; Kober, J. PUMA: Deep metric imitation learning for stable motion primitives. *Adv. Intell. Syst.* **2024**, *6*, 2400144. [CrossRef]

15. Fu, J.; Jin, Z.; Liu, A.; Zhang, W.A.; Yu, L. Non-parametric Gaussian process movement primitive with via-point constraint for effective and safe robot skill learning. *Neurocomputing* **2024**, *589*, 127711. [CrossRef]
16. Sun, J.; Feng, Q.; Zhang, Y.; Ru, M.; Li, Y.; Li, T.; Zhao, C. Fruit flexible collecting trajectory planning based on manual skill imitation for grape harvesting robot. *Comput. Electron. Agr.* **2024**, *225*, 109332. [CrossRef]
17. Lauretti, C.; Tamantini, C.; Zollo, L. A new dmp scaling method for robot learning by demonstration and application to the agricultural domain. *IEEE Access* **2024**, *12*, 7661–7673. [CrossRef]
18. Torabi, F.; Warnell, G.; Stone, P. Behavioral cloning from observation. *arXiv* **2018**, arXiv:1805.01954.
19. Triantafyllidis, E.; Acero, F.; Liu, Z.; Li, Z. Hybrid hierarchical learning for solving complex sequential tasks using the robotic manipulation network ROMAN. *Nat. Mach. Intell.* **2023**, *5*, 991–1005. [CrossRef]
20. Peng, Y.; Zeng, J.; Hu, Y.; Fang, Q.; Yin, Q. Reinforcement learning from suboptimal demonstrations based on reward relabeling. *Expert Syst. Appl.* **2024**, *255*, 124580. [CrossRef]
21. Li, X.; Wang, X.; Zheng, X.; Jin, J.; Huang, Y.; Zhang, J.J.; Wang, F.Y. SADRL: Merging human experience with machine intelligence via supervised assisted deep reinforcement learning. *Neurocomputing* **2022**, *467*, 300–309. [CrossRef]
22. Saveriano, M.; Abu-Dakka, F.J.; Kramberger, A.; Peternel, L. Dynamic movement primitives in robotics: A tutorial survey. *Int. J. Robot. Res.* **2023**, *42*, 1133–1184. [CrossRef]
23. Lu, Z.; Wang, N.; Li, Q.; Yang, C. A trajectory and force dual-incremental robot skill learning and generalization framework using improved dynamical movement primitives and adaptive neural network control. *Neurocomputing* **2023**, *521*, 146–159. [CrossRef]
24. Yue, C.; Gao, T.; Lu, L.; Lin, T.; Wu, Y. Probabilistic movement primitives based multi-task learning framework. *Comput. Ind. Eng.* **2024**, *191*, 110144. [CrossRef]
25. Khansari-Zadeh, S.M.; Billard, A. Learning stable nonlinear dynamical systems with Gaussian mixture models. *IEEE Trans. Robot.* **2011**, *27*, 943–957. [CrossRef]
26. Huang, Y.L.; Rozo, L.; Silverio, J.; Caldwell, D.G. Kernelized movement primitive. *Int. J. Robot. Res.* **2019**, *38*, 833–852. [CrossRef]
27. Huang, Y.; Abu-Dakka, F.J.; Silvério, J.; Caldwell, D.G. Toward orientation learning and adaptation in Cartesian space. *IEEE Trans. Robot.* **2020**, *37*, 82–98. [CrossRef]
28. Ruan, S.; Liu, W.; Wang, X.; Meng, X.; Chirikjian, G.S. PRIMP: Probabilistically-informed motion primitives for efficient affordance learning from demonstration. *IEEE Trans. Robot.* **2024**, *40*, 2868–2887. [CrossRef]
29. Wu, H.; Xu, Z.; Yan, W.; Ou, Y.; Liao, Z.; Zhou, X. A Framework of Rehabilitation-Assisted Robot Skill Representation, Learning, and Modulation via Manifold-Mappings and Gaussian Processes. In Proceedings of the 2022 IEEE/RSJ International Conference on Intelligent Robots and Systems (IROS), Kyoto, Japan, 23–27 October 2022.
30. Zou, C.; Huang, R.; Cheng, H.; Qiu, J. Learning gait models with varying walking speeds. *IEEE Robot. Autom. Lett.* **2020**, *6*, 183–190. [CrossRef]
31. Liu, Z.; Ai, Q.; Liu, H.; Meng, W.; Liu, Q. Human-like trajectory planning based on postural synergistic kernelized movement primitives for robot-assisted rehabilitation. *IEEE Trans. Hum.-Mach. Syst.* **2024**, *54*, 152–161. [CrossRef]
32. Pan, M.Z.; Deng, Y.W.; Li, Z.; Chen, Y.; Liao, X.L.; Bian, G.B. Dynamic multiaction recognition and expert movement mapping for closed pelvic reduction. *IEEE Trans. Ind. Inf.* **2022**, *19*, 8667–8678. [CrossRef]
33. Bian, G.B.; Chen, Z.; Li, Z.; Wang, Y.; Zhang, L. Learning surgical skills under the RCM constraint from demonstrations in robot-assisted minimally invasive surgery. *Expert Syst. Appl.* **2023**, *225*, 120134. [CrossRef]
34. Zhang, R.; Chen, J.; Wang, Z.; Yang, Z.; Ren, Y.; Shi, P.; Calo, J.; Lam, K.; Purkayastha, S.; Lo, B. A step towards conditional autonomy—Robotic appendectomy. *IEEE Robot. Autom. Lett.* **2023**, *8*, 2429–2436. [CrossRef]
35. Schwaner, K.L.; Iturrate, I.; Andersen, J.K.H.; Jensen, P.T.; Savarimuthu, T.R. Autonomous Bi-Manual Surgical Suturing Based on Skills Learned from Demonstration. In Proceedings of the 2021 IEEE/RSJ International Conference on Intelligent Robots and Systems (IROS), Prague, Czech Republic, 27 September–1 October 2021.
36. Su, H.; Mariani, A.; Ovur, S.E.; Menciassi, A.; Ferrigno, G.; De Momi, E. Toward teaching by demonstration for robot-assisted minimally invasive surgery. *IEEE Trans. Autom. Sci. Eng.* **2021**, *18*, 484–494. [CrossRef]
37. Buchli, J.; Stulp, F.; Theodorou, E.; Schaal, S. Learning variable impedance control. *Int. J. Robot. Res.* **2011**, *30*, 820–833. [CrossRef]
38. Dai, Y.; Xiang, C.; Qu, W.; Zhang, Q. A Review of End-Effector Research Based on Compliance Control. *Machines* **2022**, *10*, 100. [CrossRef]
39. Haddadin, S.; Shahriari, E. Unified force-impedance control. *Int. J. Robot. Res.* **2024**, *43*, 2112–2141. [CrossRef]
40. Zahedi, F.; Lee, H. Biomechanics-Based User-Adaptive Variable Impedance Control for Enhanced Physical Human–Robot Interaction Using Bayesian Optimization. *Adv. Intell. Syst.* **2024**, *7*, 2400333. [CrossRef]
41. Hu, J.; Zhuang, Y.; Meng, Q.; Yu, H. Active Training Control Method for Rehabilitation Robot Based on Fuzzy Adaptive Impedance Adjustment. *Machines* **2023**, *11*, 565. [CrossRef]

42. Duan, A.; Victorova, M.; Zhao, J.; Sun, Y.; Zheng, Y.; Navarro-Alarcon, D. Ultrasound-guided assistive robots for scoliosis assessment with optimization-based control and variable impedance. *IEEE Robot. Autom. Lett.* **2022**, *7*, 8106–8113. [CrossRef]
43. Chen, Y.; Zhang, Y.; Zhao, X.; Xie, Q.; Yang, K.; Tao, B.; Ding, H. Physical human–robot interaction based on adaptive impedance control for robotic-assisted total hip arthroplasty. *IEEE-ASME Trans. Mech.* **2024**, *29*, 4674–4686. [CrossRef]
44. Zheng, G.; Lei, J.; Hu, L. Fuzzy adaptive sliding mode impedance control of fracture reduction robot. *IEEE Access* **2021**, *9*, 113653–113665. [CrossRef]
45. Zheng, G.; Lei, J.; Hu, L. Adaptive variable impedance position/force tracking control of fracture reduction robot. *Int. J. Med. Robot. Comp.* **2023**, *19*, e2469. [CrossRef]
46. Wang, X.; Zhang, R.; Miao, Y.; An, M.; Wang, S.; Zhang, Y. PI²-based adaptive impedance control for gait adaption of lower limb exoskeleton. *IEEE-ASME Trans. Mech.* **2024**, *29*, 4251–4261. [CrossRef]
47. Liu, W.; Wu, R.; Si, J.; Huang, H. A new robotic knee impedance control parameter optimization method facilitated by inverse reinforcement learning. *IEEE Robot. Autom. Lett.* **2022**, *7*, 10882–10889. [CrossRef]
48. Fu, J.; Burzo, I.; Iovene, E.; Zhao, J.; Ferrigno, G.; De Momi, E. Optimization-based variable impedance control of robotic manipulator for medical contact tasks. *IEEE Trans. Instrum. Meas.* **2024**, *73*, 4004608. [CrossRef]
49. Ren, Y.; Zhou, Z.; Xu, Z.; Yang, Y.; Zhai, G.; Leibold, M.; Ni, F.; Zhang, Z.; Buss, M.; Zheng, Y. Enabling versatility and dexterity of the dual-arm manipulators: A general framework toward universal cooperative manipulation. *IEEE Trans. Robot.* **2024**, *40*, 2024–2045. [CrossRef]
50. Dio, M.; Völz, A.; Graichen, K. Cooperative Dual-Arm Control for Heavy Object Manipulation Based on Hierarchical Quadratic Programming. In Proceedings of the 2023 IEEE/RSJ International Conference on Intelligent Robots and Systems (IROS), Detroit, MI, USA, 1–5 October 2023.
51. Jiao, C.; Zhang, L.; Su, X.; Huang, J.; Bing, Z.; Knoll, A. Task-based compliance control for bottle screw manipulation with a dual-arm robot. *IEEE Trans. Ind. Electron.* **2023**, *71*, 1823–1831. [CrossRef]
52. Wang, D.; Qiu, C.; Lian, J.; Wan, W.; Pan, Q.; Dong, Y. Cooperative control for dual-arm robots based on improved dynamic movement primitives. *IEEE Trans. Ind. Electron.* **2024**. [CrossRef]
53. Bai, W.; Wang, Z.; Cao, Q.; Yokoi, H.; Fujie, M.G.; Yeatman, E.M.; Yang, G.Z. Anthropomorphic dual-arm coordinated control for a single-port surgical robot based on dual-step optimization. *IEEE Trans. Med. Robot. Bio.* **2022**, *4*, 72–84. [CrossRef]
54. Ferraguti, F.; Preda, N.; Manurung, A.; Bonfe, M.; Lambercy, O.; Gassert, R.; Muradore, R.; Fiorini, P.; Secchi, C. An energy tank-based interactive control architecture for autonomous and teleoperated robotic surgery. *IEEE Trans. Robot.* **2015**, *31*, 1073–1088. [CrossRef]
55. Zhang, H.; Pang, L.; Bai, M.; Yang, J.; Zhao, J. Retinal surgical field realignment based on master-slave dual-arm surgical robot. *IEEE Trans. Autom. Sci. Eng.* **2023**, *21*, 4743–4752. [CrossRef]
56. Jinjun, D.; Yahui, G.; Ming, C.; Xianzhong, D. Symmetrical adaptive variable admittance control for position/force tracking of dual-arm cooperative manipulators with unknown trajectory deviations. *Robot. Cim-Int. Manuf.* **2019**, *57*, 357–369. [CrossRef]
57. Jiao, C.; Yu, L.; Su, X.; Wen, Y.; Dai, X. Adaptive hybrid impedance control for dual-arm cooperative manipulation with object uncertainties. *Automatica* **2022**, *140*, 110232. [CrossRef]
58. Yan, L.; Yang, Y.; Xu, W.; Vijayakumar, S. Dual-Arm Coordinated Motion Planning and Compliance Control for Capturing Moving Objects with Large Momentum. In Proceedings of the 2019 IEEE/RSJ International Conference on Intelligent Robots and Systems (IROS), Madrid, Spain, 1–5 October 2019.
59. Walker, I.D.; Freeman, R.A.; Marcus, S.I. Analysis of motion and internal loading of objects grasped by multiple cooperating manipulators. *Int. J. Robot. Res.* **1991**, *10*, 396–409. [CrossRef]
60. Zhou, F.; Torre, F.D.L. Generalized canonical time warping. *IEEE Trans. Pattern. Anal.* **2016**, *38*, 279–294. [CrossRef]
61. Mitchel, T.W.; Ruan, S.; Chirikjian, G.S. Signal Alignment for Humanoid Skeletons via the Globally Optimal Reparameterization Algorithm. In Proceedings of the 2018 IEEE-RAS 18th International Conference on Humanoid Robots (Humanoids), Beijing, China, 6–9 November 2018.
62. Leite, A.C.; Lizarralde, F.; Hsu, L. A Cascaded-Based Hybrid Position-Force Control for Robot Manipulators with Nonnegligible Dynamics. In Proceedings of the IEEE 2010 American Control Conference (ACC), Baltimore, MD, USA, 30 June–2 July 2010.
63. Ju, M.S.; Lin, C.C.K.; Lin, D.H.; Hwang, I.S.; Chen, S.M. A rehabilitation robot with force-position hybrid fuzzy controller: Hybrid fuzzy control of rehabilitation robot. *IEEE Trans. Neur. Sys. Reh.* **2005**, *13*, 349–358.
64. Hogan, N. Impedance control: An Approach to Manipulation. In Proceedings of the IEEE 1984 American Control Conference (ACC), San Diego, CA, USA, 6–8 June 1984; pp. 304–313.
65. Ott, C.; Albu-Schäffer, A.; Kugi, A.; Stramigioli, S.; Hirzinger, G. A Passivity-Based Cartesian Impedance Controller for Flexible Joint Robots—Part I: Torque Feedback and Gravity Compensation. In Proceedings of the 2004 IEEE International Conference on Robotics and Automation (ICRA), New Orleans, LA, USA, 26 April–1 May 2004; pp. 2659–2665.

66. Zhu, S.; Zhao, Z.; Chen, Y.; Zhang, J.; Wang, J. Development of a Surgeon- and Patient-Friendly Orthopedic Surgical Robot. In Proceedings of the IEEE 2021 International Symposium on Medical Robotics (ISMR), Atlanta, GA, USA, 17–19 November 2021; pp. 1–6.
67. Tang, P.; Hu, L.; Du, H.; Gong, M.; Zhang, L. Novel 3D hexapod computer-assisted orthopaedic surgery system for closed diaphyseal fracture reduction. *Int. J. Med.Robot. Comput. Assist. Surg.* **2012**, *8*, 17–24. [CrossRef]

Disclaimer/Publisher's Note: The statements, opinions and data contained in all publications are solely those of the individual author(s) and contributor(s) and not of MDPI and/or the editor(s). MDPI and/or the editor(s) disclaim responsibility for any injury to people or property resulting from any ideas, methods, instructions or products referred to in the content.